

Variant of gas kinetic flux solver for flows beyond Navier-Stokes level

Z. Y. Yuan ¹, C. Shu ^{1,*}, Z. J. Liu ¹, L. M. Yang ², and W. Liu ¹

¹*Department of Mechanical Engineering, National University of Singapore, 10 Kent Ridge Crescent, 119260, Singapore*

²*Department of Aerodynamics, Nanjing University of Aeronautics and Astronautics, Nanjing 210016, China*



(Received 20 July 2021; accepted 18 October 2021; published 16 November 2021)

In this paper, a variant of gas kinetic flux solver (GKFS) is presented for simulation of flows beyond the Navier-Stokes (NS) level. The method retains the framework of GKFS and reconstructs the numerical fluxes by the moments of distribution function at the cell interface, which is given from the local solution of the Boltzmann equation. In the conventional GKFS, the first-order Chapman-Enskog (CE) expansion is utilized to approximate the initial distribution function. By using the differential chain rule, it was found that the CE expansion form could be linked to the stress tensor and the heat flux. For flows in the NS level, the stress tensor and heat flux can be simply calculated from the linearized constitutive relationship and Fourier's law, respectively. However, for flows beyond the NS level, due to the strong nonequilibrium effect, the linearized constitutive relationship and Fourier's law are insufficient to predict the stress tensor and the heat flux. To overcome this difficulty, this paper introduces correction terms to the stress tensor and heat flux in the initial distribution function. These correction terms will take effect in the strong nonequilibrium region for flows beyond the NS level. To avoid finding complex expressions or solving complicated partial differential equations for the correction terms, a simple and iterative procedure is proposed to update the correction terms based on the framework of GKFS. The proposed method is validated by three benchmark cases which cover the flow from the continuum regime to the transition regime. Numerical results show that the present solver can provide accurate solution in the continuum regime. It is indeed the correction terms that take effect in the strong nonequilibrium region for flows beyond the NS level, which enables the present solver to capture the nonequilibrium phenomenon with reasonable accuracy for rarefied flows at moderate Knudsen number.

DOI: [10.1103/PhysRevE.104.055305](https://doi.org/10.1103/PhysRevE.104.055305)

I. INTRODUCTION

In recent years, various kinds of gas kinetic solvers have been developed as an alternative approach to study the fluid flow problem both in academic exploration and in industrial applications. These methods can be generally classified into three categories: the first one is the kinetic flux vector splitting scheme [1–4], and the improved version developed by Chou and Baganoff [4] contains two stages: free transport and collision. Because the collisionless part and the collision part of the Boltzmann equation are solved separately for flux evaluation, this scheme is only capable for flow problems where physical viscosity is much larger than numerical viscosity. The second type of scheme is the gas kinetic scheme [5–9] (GKS), which includes the Bhatnagar-Gross-Krook (BGK) collision term in the evaluation of numerical flux at the cell interface. In GKS, the use of local integral solution to the Boltzmann equation naturally combines the streaming and collision processes together. The third type of scheme is the gas kinetic flux solver [10–14] (GKFS). Different from the GKS, the local solution of Boltzmann equation along the characteristic line is adopted for evaluation of numerical flux at the cell interface.

The nice feature of all the above three schemes is the physical reconstruction of numerical fluxes. In GKFS, the viscous and inviscid fluxes at the cell interface are evaluated simultaneously by the moments of distribution function, which is given from the local solution of Boltzmann equation and evolved from the initial distribution function at the neighboring points of cell interface. At the same time, this distribution function couples the transport and collision processes of gas molecules. Thus, the time step is not restricted to the particle collision time and merely determined by the Courant-Friedrichs-Lewy (CFL) condition. In GKFS, the initial distribution function is approximated with the help of the first-order Chapman-Enskog (CE) expansion. To the Navier-Stokes (NS) level, the initial distribution function can be expressed as $f^{\text{NS}} = f^{\text{eq}} - \tau D f^{\text{eq}}$, where f^{eq} is the equilibrium part of distribution function, τ is the relaxation time, and D represents the substantial derivative. In Ref. [9], the nonequilibrium part of $-\tau D f^{\text{eq}}$ is approximated by the finite difference scheme, which introduces some numerical error into the computation. As shown in this paper, by using differential chain rule, the nonequilibrium part for Newtonian fluid can be explicitly expressed as the function of velocity and temperature gradients. Furthermore, the velocity gradient can be replaced by the stress tensor $\sigma_{ij} = -2\mu(\partial U_{<i}/\partial x_{j>})$ using the linearized constitutive relationship and the temperature gradient is replaced by the heat flux $q_i = -\lambda(\partial T/\partial x_i)$ using Fourier's law, where μ and λ represent the viscosity and

*mpeshuc@nus.edu.sg

thermal conductivity, respectively. This finding gives us a hint that the CE expansion can accurately recover the macroscopic NS equations since the nonequilibrium part of the gas distribution function indeed satisfies the linearized constitutive relationship for stress tensor and Fourier's law for heat flux. At the same time, this may also imply that GKFS may be inadequate for flows beyond the NS level as the strong nonequilibrium effect cannot be simply considered by the linearized constitutive relationship and Fourier's law.

To extend the conventional gas kinetic scheme for flows beyond NS level, the unified gas kinetic scheme [15,16] and discrete unified gas kinetic scheme [17,18] are proposed, subsequently. These two methods are both reliable for flows beyond NS level, because their initial distribution functions are not approximated by the CE expansion, but calculated through the evolution functions. However, this evolution process requires additional discretization in the phase velocity space, which leads to the additional computational cost. To avoid the evolution of gas distribution function, its explicit formulation that can simulate flows beyond NS level should be addressed. Considering the fact that the stress tensor and heat flux actually reflect the degree of nonequilibrium effect, some efforts [19–22] have been made to introduce high-order constitutive relations for simulation of flows beyond the NS level. The extended gas kinetic scheme [23] (EGKS) is such an attempt by adopting the high-order constitutive relations in the gas distribution function as an extension of GKS. High-order constitutive relations, such as Burnett [24,25], simplified conventional Burnett [26,27], regularized Chapman-Enskog expansion [28], and nonlinear coupled constitutive relations (NCCR) [29,30] are all tested in the framework of EGKS. The EGKS method shows usefulness of high-order constitutive relations in the gas distribution function for nonequilibrium flows beyond the NS level. On the other hand, it should be indicated that the high-order constitutive relations may have very complicated expressions or need to solve additional partial differential equations. This brings difficulty in numerical implementation.

To effectively consider the strong nonequilibrium effect for flows beyond the NS level, in this paper we introduce the correction terms to stress tensor and heat flux in the initial gas distribution function. The correction terms are treated as a compensation to the inadequate NS constitutive relations and take effect in the strong nonequilibrium regime for flows beyond the NS level. From the perspective of Burnett-type equations [25,26], these correction terms are equivalent to the second-order or third-order derivatives of macroscopic variables. In the NCCR formulations [30,31], these correction terms are equal to the additional algebraic nonlinear terms. For the moment methods [20,32], these correction terms take effect as the high-order moments to some extent. Naturally, one may pursue the explicit expressions for the correction terms as done by EGKS for the high-order constitutive relations. However, as discussed above, the explicit expressions will be very complicated and implementation may encounter numerical instability. To resolve this difficulty, a natural question is whether the correction terms could be treated in a simple and general way. The recent work of a novel solver [33,34] provides an answer to this question.

Unlike the conventional moment methods [20,32], where the moments including the stress tensor and heat flux are given by solving a set of complicated partial differential equations, the novel solver starts from the kinetic theory and determines the moments by moment relationship of the distribution function.

Inspired by the novel solver, we propose a variant of GKFS in this work for simulating flows from the continuum regime to the rarefied regime at moderate Knudsen number. In the present solver, the initial distribution function of GKFS is modified by introducing the correction terms to the stress tensor and heat flux. In other words, the stress tensor and heat flux for flows beyond the NS level are expressed as $\sigma_{ij} = -2\mu(\partial U_{<i/\partial x_{j>}) + \Delta_{ij}$ and $q_i = -\lambda(\partial T/\partial x_i) + \Delta_i$, where Δ_{ij} and Δ_i are the correction terms. As discussed above, it is very difficult to get explicit expressions for Δ_{ij} and Δ_i . However, in the framework of GKFS, they can be easily obtained by an iterative process. The basic idea is that the correction terms are actually the differences between actual stress tensor–heat flux and stress tensor–heat flux given from linearized constitutive relationship and Fourier's law (they can be termed as NS stress tensor–heat flux). From the kinetic theory, the actual stress tensor and heat flux can be calculated by moment integrals of distribution function. The essence of GKFS is to reconstruct the distribution function at each cell interface and then use it to compute the macroscopic flow variables and fluxes through moment relationships of distribution function. This idea can also be extended to compute the actual stress tensor–heat flux at the cell interface once the distribution function is reconstructed. In the meantime, the NS stress tensor and heat flux can be easily obtained from the velocity and temperature gradients. Therefore, it is straightforward to get the correction terms at each cell interface by comparing the difference between the actual stress tensor–heat flux and the NS stress tensor–heat flux. For a control cell, once the correction terms at all cell interfaces are available, they can be used to get the correction terms at the cell center through interpolation. The above procedure forms an iterative process to update the correction terms. Through this way, finding complicated expressions or solving additional partial differential equations for the correction terms is avoided. This part is the major contribution of the present paper, and its details will be given in Sec. IV. The proposed solver is validated by three test examples. Numerical results show that the present solver can work well for flows not only in the continuum region but also in the transition region. It is indeed the correction terms that take effect in the strong nonequilibrium region for the flows beyond the NS level.

The rest of the paper is organized as follows. In Sec. II, some brief description on relationships between macroscopic flow variables and gas distribution function of Boltzmann equation is presented. Section III discusses reconstruction of distribution function at cell interface and approximation of initial distribution function. The details of gas kinetic flux solver for flows beyond the NS level are described in Sec. IV. Three typical numerical examples, including planar Couette flow, lid-driven cavity flow, and heat transfer in a bottom-heated square cavity, are presented in Sec. V. Finally, Sec. VI draws some conclusions.

II. RELATIONSHIPS OF MACROSCOPIC CONSERVATIVE VARIABLES AND FLUXES WITH DISTRIBUTION FUNCTION OF BOLTZMANN EQUATION

At the mesoscopic level, the fluid flow can be modeled by the Boltzmann equation. The 2D gas-kinetic governing equation with BGK collision model [35] for monatomic gas can be written as

$$\frac{\partial f}{\partial t} + \boldsymbol{\xi} \cdot \nabla f = \frac{f^{\text{eq}} - f}{\tau}, \quad (1)$$

where f and f^{eq} are the gas distribution function and its equilibrium state, respectively. $\boldsymbol{\xi} = (u, v, w)$ represents the particle velocity space. In 2D case, w can be treated as the particle's internal degree of freedom, and for simplicity, it is noted as η . τ denotes the relaxation time and is related to the dynamic viscosity and pressure. The equilibrium state is given by the Maxwellian distribution function, as shown below:

$$f^{\text{eq}} = \rho \left(\frac{\lambda}{\pi} \right)^{3/2} e^{-\lambda[(u-U)^2 + (v-V)^2 + \eta^2]}. \quad (2)$$

Here, ρ is the macroscopic density and $\lambda = 1/2RT$, where R is the gas constant and T is the macroscopic temperature. U and V are macroscopic velocity components in the x and y directions, respectively.

Note that the evolution of distribution function f above depends only on the particle velocity $\mathbf{u} = (u, v)$ and is irrelevant to the internal degree of freedom η . To remove the phase-energy variable η and develop more compact formulations, the double-distribution functions h and b are introduced [36] as below:

$$h(\mathbf{x}, \mathbf{u}, t) = \int f(\mathbf{x}, \mathbf{u}, \eta, t) d\eta, \quad (3)$$

$$b(\mathbf{x}, \mathbf{u}, t) = \int \eta^2 f(\mathbf{x}, \mathbf{u}, \eta, t) d\eta. \quad (4)$$

Subsequently, the double-distribution functions $h^{\text{eq}}(\mathbf{x}, \mathbf{u}, t)$ and $b^{\text{eq}}(\mathbf{x}, \mathbf{u}, t)$ at equilibrium state can be written as

$$h^{\text{eq}}(\mathbf{x}, \mathbf{u}, t) = \int f^{\text{eq}}(\mathbf{x}, \mathbf{u}, \eta, t) d\eta = \frac{\rho\lambda}{\pi} e^{-\lambda[(u-U)^2 + (v-V)^2]}, \quad (5)$$

$$b^{\text{eq}}(\mathbf{x}, \mathbf{u}, t) = \int \eta^2 f^{\text{eq}}(\mathbf{x}, \mathbf{u}, \eta, t) d\eta = \frac{\rho}{2\pi} e^{-\lambda[(u-U)^2 + (v-V)^2]}. \quad (6)$$

As a result, the evolution function of f shown in Eq. (1) can be transformed into the following evolution functions of h and b as

$$\frac{\partial h}{\partial t} + \mathbf{u} \cdot \nabla h = \frac{h^{\text{eq}} - h}{\tau}, \quad (7)$$

$$\frac{\partial b}{\partial t} + \mathbf{u} \cdot \nabla b = \frac{b^{\text{eq}} - b}{\tau}. \quad (8)$$

Multiplying Eq. (7) by the moment vector $\boldsymbol{\varphi}$,

$$\boldsymbol{\varphi} = [1, u, v, 0.5(u^2 + v^2)]^T \quad (9)$$

and then integrating the resultant equation and Eq. (8) in the particle velocity space, the following macroscopic governing

equations can be derived:

$$\frac{\partial \mathbf{W}}{\partial t} + \nabla \cdot \mathbf{F} = 0, \quad (10)$$

where \mathbf{W} is the vector of macroscopic conservative variables $\mathbf{W} = (\rho, \rho U, \rho V, \rho E)^T$, which can be computed by the double-distribution functions h and b as

$$\rho = \langle h(\mathbf{x}, \mathbf{u}, t) \rangle, \quad (11)$$

$$\rho U = \langle uh(\mathbf{x}, \mathbf{u}, t) \rangle, \quad (12)$$

$$\rho V = \langle vh(\mathbf{x}, \mathbf{u}, t) \rangle, \quad (13)$$

$$\rho E = \frac{1}{2} \langle \mathbf{u}^2 h(\mathbf{x}, \mathbf{u}, t) + b(\mathbf{x}, \mathbf{u}, t) \rangle. \quad (14)$$

The total energy E is calculated by

$$E = \frac{1}{2}(U^2 + V^2) + \frac{RT}{\gamma - 1}, \quad (15)$$

in which γ is the specific-heat ratio and equal to 5/3 for monatomic gas. In Eqs. (11)–(14), the operator $\langle \dots \rangle$ is defined as

$$\langle \dots \rangle = \int_{-\infty}^{+\infty} \int_{-\infty}^{+\infty} (\dots) d\mathbf{u}. \quad (16)$$

In addition, the flux vector \mathbf{F} is $\mathbf{F} = (\mathbf{F}^x, \mathbf{F}^y)$ for the 2D case. The relationship between $\mathbf{F}^x = (F_{\rho}^x, F_{\rho U}^x, F_{\rho V}^x, F_{\rho E}^x)^T$ and double-distribution functions can be written as

$$F_{\rho}^x = \langle uh(\mathbf{x}, \mathbf{u}, t) \rangle, \quad (17)$$

$$F_{\rho U}^x = \langle u^2 h(\mathbf{x}, \mathbf{u}, t) \rangle, \quad (18)$$

$$F_{\rho V}^x = \langle uvh(\mathbf{x}, \mathbf{u}, t) \rangle, \quad (19)$$

$$F_{\rho E}^x = \frac{1}{2} \langle u[(u^2 + v^2)h(\mathbf{x}, \mathbf{u}, t) + b(\mathbf{x}, \mathbf{u}, t)] \rangle. \quad (20)$$

Similarly, $\mathbf{F}^y = (F_{\rho}^y, F_{\rho U}^y, F_{\rho V}^y, F_{\rho E}^y)^T$ can be computed by

$$F_{\rho}^y = \langle vh(\mathbf{x}, \mathbf{u}, t) \rangle, \quad (21)$$

$$F_{\rho U}^y = \langle uvh(\mathbf{x}, \mathbf{u}, t) \rangle, \quad (22)$$

$$F_{\rho V}^y = \langle v^2 h(\mathbf{x}, \mathbf{u}, t) \rangle, \quad (23)$$

$$F_{\rho E}^y = \frac{1}{2} \langle v[(u^2 + v^2)h(\mathbf{x}, \mathbf{u}, t) + b(\mathbf{x}, \mathbf{u}, t)] \rangle. \quad (24)$$

By applying the finite volume method to discretize Eq. (10), the discrete governing equations at the macroscopic scale can be expressed as

$$\frac{d\mathbf{W}_i}{dt} + \frac{1}{\Omega_i} \sum_{n=1}^N \mathbf{F}_n S_n = 0 \quad (25)$$

where \mathbf{W}_i is the vector of conservative variables at the cell center i . Ω_i represents the volume and N represents the number of control surfaces. S_n and \mathbf{F}_n stand for the area and flux vector at the cell interface n . Equation (25) can be applied for flows in both the continuum regime and the rarefied regime. The GKFS uses the distribution functions at the cell interface to evaluate the flux vector \mathbf{F} by using Eqs. (17)–(24). The

computation of distribution function at the cell interface will be addressed in the next section.

III. DISTRIBUTION FUNCTION AT CELL INTERFACE AND APPROXIMATION OF INITIAL DISTRIBUTION FUNCTION

It is noteworthy that the BGK equation is the cornerstone for the gas kinetic theory. In this section, we will discuss how to determine the distribution function at the cell interface from the gas kinetic BGK model [35]. Furthermore, we will discuss approximation of initial gas distribution function associated with the solution of distribution function at the cell interface.

A. Determination of distribution function at cell interface by Boltzmann equation

At first, the distribution function h and its equilibrium state h^{eq} at the midpoint of a cell interface \mathbf{x}_f and at time step $t + \delta t$ are noted as $h(\mathbf{x}_f, \mathbf{u}, t + \delta t)$ and $h^{\text{eq}}(\mathbf{x}_f, \mathbf{u}, t + \delta t)$, respectively. The distribution function h at the surrounding points of \mathbf{x}_f at time step t is written as $h(\mathbf{x}_f - \mathbf{u}\delta t, \mathbf{u}, t)$. Hence, the left-hand side of Eq. (7) can be approximated as

$$\frac{\partial h}{\partial t} + \mathbf{u} \cdot \nabla h = \frac{h(\mathbf{x}_f, \mathbf{u}, t + \delta t) - h(\mathbf{x}_f - \mathbf{u}\delta t, \mathbf{u}, t)}{\delta t}. \quad (26)$$

At the same time, the right-hand side of Eq. (7) can be written as

$$\frac{h^{\text{eq}} - h}{\tau} = \frac{h^{\text{eq}}(\mathbf{x}_f, \mathbf{u}, t + \delta t) - h(\mathbf{x}_f, \mathbf{u}, t + \delta t)}{\tau}. \quad (27)$$

By substituting Eq. (26) and Eq. (27) into Eq. (7), the distribution function $h(\mathbf{x}_f, \mathbf{u}, t + \delta t)$ at the cell interface can be computed by

$$h(\mathbf{x}_f, \mathbf{u}, t + \delta t) = \frac{\tau}{\tau + \delta t} h(\mathbf{x}_f - \mathbf{u}\delta t, \mathbf{u}, t) + \frac{\delta t}{\tau + \delta t} h^{\text{eq}}(\mathbf{x}_f, \mathbf{u}, t + \delta t). \quad (28)$$

This equation reveals that the distribution function h at the cell interface is a combination of the distribution function at the surrounding points of the interface \mathbf{x}_f and the equilibrium distribution function at the cell interface. Similarly, the distribution function $b(\mathbf{x}_f, \mathbf{u}, t + \delta t)$ at the cell interface can be calculated by the following form:

$$b(\mathbf{x}_f, \mathbf{u}, t + \delta t) = \frac{\tau}{\tau + \delta t} b(\mathbf{x}_f - \mathbf{u}\delta t, \mathbf{u}, t) + \frac{\delta t}{\tau + \delta t} b^{\text{eq}}(\mathbf{x}_f, \mathbf{u}, t + \delta t). \quad (29)$$

As shown in Eqs. (28) and (29), to get the double-distribution functions $h(\mathbf{x}_f, \mathbf{u}, t + \delta t)$ and $b(\mathbf{x}_f, \mathbf{u}, t + \delta t)$ at the cell interface, one has to know the equilibrium distribution functions $h^{\text{eq}}(\mathbf{x}_f, \mathbf{u}, t + \delta t)$ and $b^{\text{eq}}(\mathbf{x}_f, \mathbf{u}, t + \delta t)$ at the cell interface, and the initial distribution functions at the surrounding points of the cell interface, $h(\mathbf{x}_f - \mathbf{u}\delta t, \mathbf{u}, t)$ and $b(\mathbf{x}_f - \mathbf{u}\delta t, \mathbf{u}, t)$. Equations (5) and (6) reveal that once the macroscopic flow variables ρ , U , V , and T are determined, h^{eq} and b^{eq} can be uniquely decided. Thus, the key step is to approximate $h(\mathbf{x}_f - \mathbf{u}\delta t, \mathbf{u}, t)$ and $b(\mathbf{x}_f - \mathbf{u}\delta t, \mathbf{u}, t)$, which

are initial distribution functions at the surrounding points of the cell interface.

B. Approximation of initial distribution function for flows in the NS level

In the conventional GKFS [37], which is targeted to simulate flows in the Navier-Stokes level, the initial distribution functions $h(\mathbf{x}_f - \mathbf{u}\delta t, \mathbf{u}, t)$ and $b(\mathbf{x}_f - \mathbf{u}\delta t, \mathbf{u}, t)$ are approximated by the first-order CE expansion [38–41] and are given as

$$h^{\text{NS}}(\mathbf{x}_f - \mathbf{u}\delta t, \mathbf{u}, t) = h^{\text{eq}}(\mathbf{x}_f - \mathbf{u}\delta t, \mathbf{u}, t) - \tau Dh^{\text{eq}}(\mathbf{x}_f - \mathbf{u}\delta t, \mathbf{u}, t), \quad (30)$$

$$b^{\text{NS}}(\mathbf{x}_f - \mathbf{u}\delta t, \mathbf{u}, t) = b^{\text{eq}}(\mathbf{x}_f - \mathbf{u}\delta t, \mathbf{u}, t) - \tau Db^{\text{eq}}(\mathbf{x}_f - \mathbf{u}\delta t, \mathbf{u}, t). \quad (31)$$

The second terms on the right-hand side of Eqs. (30) and (31) are the approximation of the nonequilibrium part of distribution function. As shown in Refs. [37] and [42], the substantial derivatives Dh^{eq} and Db^{eq} can be approximated by the following finite difference scheme:

$$Dh^{\text{eq}}(\mathbf{x}_f - \mathbf{u}\delta t, \mathbf{u}, t) = \frac{h^{\text{eq}}(\mathbf{x}_f, \mathbf{u}, t + \delta t) - h^{\text{eq}}(\mathbf{x}_f - \mathbf{u}\delta t, \mathbf{u}, t)}{\delta t}, \quad (32)$$

$$Db^{\text{eq}}(\mathbf{x}_f - \mathbf{u}\delta t, \mathbf{u}, t) = \frac{b^{\text{eq}}(\mathbf{x}_f, \mathbf{u}, t + \delta t) - b^{\text{eq}}(\mathbf{x}_f - \mathbf{u}\delta t, \mathbf{u}, t)}{\delta t}. \quad (33)$$

It is noted that this approximation introduces numerical errors into the computation. Another way to compute the substantial derivative of distribution function at equilibrium state can be made by performing the differential chain rule as follows:

$$Dh^{\text{eq}} = \frac{\partial h^{\text{eq}}}{\partial \rho} D\rho + \frac{\partial h^{\text{eq}}}{\partial U_i} DU_i + \frac{\partial h^{\text{eq}}}{\partial T} DT, \quad (34)$$

$$Db^{\text{eq}} = \frac{\partial b^{\text{eq}}}{\partial \rho} D\rho + \frac{\partial b^{\text{eq}}}{\partial U_i} DU_i + \frac{\partial b^{\text{eq}}}{\partial T} DT. \quad (35)$$

Based on the double-distribution functions at equilibrium state shown in Eqs. (5) and (6), the partial derivative of equilibrium distribution function such as $\partial h^{\text{eq}}/\partial \rho$, $\partial h^{\text{eq}}/\partial U_i$, and $\partial h^{\text{eq}}/\partial T$ can be given out explicitly. Furthermore, using Euler equations, $D\rho$, DU_i , and DT can also be given explicitly [43,44]. Therefore, explicit formulations of Dh^{eq} and Db^{eq} can be derived and the final explicit formulations of $h^{\text{NS}}(\mathbf{x}_f - \mathbf{u}\delta t, \mathbf{u}, t)$ and $b^{\text{NS}}(\mathbf{x}_f - \mathbf{u}\delta t, \mathbf{u}, t)$ can be given out as

$$h^{\text{NS}} = h^{\text{eq}} - \tau h^{\text{eq}} \times \left\{ \lambda \left[C_x^2 \left(\frac{4}{3} \frac{\partial U}{\partial x} - \frac{2}{3} \frac{\partial V}{\partial y} \right) + 2C_x C_y \left(\frac{\partial U}{\partial y} + \frac{\partial V}{\partial x} \right) \right] \right. \\ \left. + \frac{1}{T} \left(C_x \frac{\partial T}{\partial x} + C_y \frac{\partial T}{\partial y} \right) \left[\lambda \left(C_x^2 + C_y^2 + \frac{1}{2\lambda} \right) - \frac{5}{2} \right] \right\}, \quad (36)$$

$$b^{\text{NS}} = b^{\text{eq}} - \tau b^{\text{eq}} \times \left\{ \lambda \left[C_x^2 \left(\frac{4}{3} \frac{\partial U}{\partial x} - \frac{2}{3} \frac{\partial V}{\partial y} \right) + 2C_x C_y \left(\frac{\partial U}{\partial y} + \frac{\partial V}{\partial x} \right) \right] \right. \\ \left. + \frac{1}{T} (C_x \frac{\partial T}{\partial x} + C_y \frac{\partial T}{\partial y}) \left[\lambda (C_x^2 + C_y^2 + \frac{3}{2\lambda}) - \frac{5}{2} \right] \right\}, \quad (37)$$

in which $C_x = u-U$ and $C_y = v-V$ represent the peculiar velocities of gas particles. The relaxation time τ is defined as the ratio of dynamic viscosity μ and pressure p and calculated by

$$\tau = \frac{\mu}{p}. \quad (38)$$

On the other hand, with the help of double-distribution functions h^{NS} and b^{NS} shown in Eqs. (36) and (37) and moment relationships, the expression of stress tensor and heat flux to the NS level can be calculated as

$$\sigma_{xx}^{\text{NS}} = \frac{1}{3} \langle (2C_x^2 - C_y^2) h^{\text{NS}} - b^{\text{NS}} \rangle = -\frac{4\mu}{3} \frac{\partial U}{\partial x} + \frac{2\mu}{3} \frac{\partial V}{\partial y}, \quad (39)$$

$$\sigma_{xy}^{\text{NS}} = \langle C_x C_y h^{\text{NS}} \rangle = -\mu \left(\frac{\partial U}{\partial y} + \frac{\partial V}{\partial x} \right), \quad (40)$$

$$\sigma_{yy}^{\text{NS}} = \frac{1}{3} \langle (2C_y^2 - C_x^2) h^{\text{NS}} - b^{\text{NS}} \rangle = -\frac{4\mu}{3} \frac{\partial V}{\partial y} + \frac{2\mu}{3} \frac{\partial U}{\partial x}, \quad (41)$$

$$\sigma_{zz}^{\text{NS}} = -\sigma_{xx}^{\text{NS}} - \sigma_{yy}^{\text{NS}} = \frac{2\mu}{3} \left(\frac{\partial U}{\partial x} + \frac{\partial V}{\partial y} \right), \quad (42)$$

$$q_x^{\text{NS}} = \frac{1}{2} \langle C_x [(C_x^2 + C_y^2) h^{\text{NS}} + b^{\text{NS}}] \rangle = -\frac{5\mu}{4\lambda T} \frac{\partial T}{\partial x}, \quad (43)$$

$$q_y^{\text{NS}} = \frac{1}{2} \langle C_y [(C_x^2 + C_y^2) h^{\text{NS}} + b^{\text{NS}}] \rangle = -\frac{5\mu}{4\lambda T} \frac{\partial T}{\partial y}. \quad (44)$$

Indeed, these relationships are exactly the same as those given from linearized constitutive relations and Fourier's law for Newtonian fluid when deriving NS equations. Using Eqs. (39)–(44), the expressions of h^{NS} and b^{NS} can be further written as

$$h^{\text{NS}} = h^{\text{eq}} \left\{ 1 + \frac{\lambda}{p} (C_x^2 \sigma_{xx}^{\text{NS}} + 2C_x C_y \sigma_{xy}^{\text{NS}} + C_y^2 \sigma_{yy}^{\text{NS}} + \frac{1}{2\lambda} \sigma_{zz}^{\text{NS}}) \right. \\ \left. + \frac{4\lambda}{5p} (C_x q_x^{\text{NS}} + C_y q_y^{\text{NS}}) \left[\lambda (C_x^2 + C_y^2 + \frac{1}{2\lambda}) - \frac{5}{2} \right] \right\}, \quad (45)$$

$$b^{\text{NS}} = b^{\text{eq}} \left\{ 1 + \frac{\lambda}{p} (C_x^2 \sigma_{xx}^{\text{NS}} + 2C_x C_y \sigma_{xy}^{\text{NS}} + C_y^2 \sigma_{yy}^{\text{NS}} + \frac{3}{2\lambda} \sigma_{zz}^{\text{NS}}) \right. \\ \left. + \frac{4\lambda}{5p} (C_x q_x^{\text{NS}} + C_y q_y^{\text{NS}}) \left[\lambda (C_x^2 + C_y^2 + \frac{3}{2\lambda}) - \frac{5}{2} \right] \right\}. \quad (46)$$

Equations (45) and (46) show that to the NS level, the double-distribution functions can be approximated by stress tensor and heat flux, which are given explicitly by Eqs. (39)–(44) in terms of velocity and temperature gradients. Since the nonequilibrium part of the distribution function is responsible

for contribution to the stress tensor and heat flux, this means that the nonequilibrium part of distribution function approximated by the first-order Chapman-Enskog expansion can well recover the stress tensor and heat flux in the NS equations. To consider flows beyond the NS level, the nonequilibrium effect is much stronger than that in the NS level, and for this case, the stress tensor and heat flux cannot be simply calculated by Eqs. (39)–(44). We will address this issue in the next section.

C. Approximation of initial distribution function for flows beyond the NS level

Many research works [19–21,45–47] have pointed out that NS equations are inadequate for flows beyond the continuum regime and the stress tensor cannot be simply calculated by the linearized constitutive relationships. Some efforts have been made to overcome this shortcoming by revising the constitutive relationships [20,25,48–50]. In the Burnett-type equations [25], except for the first-order derivatives of velocity and temperature, the second-order or third-order derivatives of macroscopic variables are additionally introduced. In the NCCR formulations [51], some additional algebraic nonlinear terms are involved. In the moment methods [52], the high-order moments are introduced, which are given by solving a set of partial differential equations. These high-order derivatives, additional algebraic nonlinear terms, and high-order moments all function as the correction terms to the linearized constitutive relations, which are the essence for better performance of Burnett-type, NCCR, and moment equations. Based on this recognition, in this work, additional correction terms are introduced to the NS expressions given by Eqs. (39)–(44). Thus, the new solver could consider the stronger nonequilibrium effect on the stress tensor and heat flux for flows beyond the NS level. As such, the modified stress tensor and heat flux are written as

$$\sigma_{ij}^{\text{modified}} = -2\mu \frac{\partial U_{<i}}{\partial x_{j>}} + \Delta_{ij}, \quad (47)$$

$$q_i^{\text{modified}} = -\frac{5\mu}{4\lambda T} \frac{\partial T}{\partial x_i} + \Delta_i, \quad (48)$$

where

$$\frac{\partial U_{<i}}{\partial x_{j>}} = \frac{1}{2} \left(\frac{\partial U_i}{\partial x_j} + \frac{\partial U_j}{\partial x_i} \right) - \frac{1}{3} \frac{\partial U_k}{\partial x_k} \delta_{ij}. \quad (49)$$

Δ_{ij} and Δ_i are the correction terms for the stress tensor and heat flux, respectively. For the 2D case, $\sigma_{ij}^{\text{modified}}$ and q_i^{modified} can be written into a tensor form as

$$[\sigma_{ij}^{\text{modified}}] = \begin{bmatrix} \sigma_{xx}^{\text{NS}} + \Delta_{xx} & \sigma_{xy}^{\text{NS}} + \Delta_{xy} & 0 \\ \sigma_{yx}^{\text{NS}} + \Delta_{yx} & \sigma_{yy}^{\text{NS}} + \Delta_{yy} & 0 \\ 0 & 0 & \sigma_{zz}^{\text{NS}} + \Delta_{zz} \end{bmatrix}, \quad (50)$$

$$[q_i^{\text{modified}}] = [q_x + \Delta_x \quad q_y + \Delta_y]. \quad (51)$$

Accordingly, the distribution functions h^{NS} and b^{NS} for NS flows shown in Eq. (45) and Eq. (46) could be modified into the expressions below:

$$h^{\text{modified}} = h^{\text{eq}} \left\{ 1 + \frac{\lambda}{p} (C_x^2 (\sigma_{xx}^{\text{NS}} + \Delta_{xx}) + 2C_x C_y (\sigma_{xy}^{\text{NS}} + \Delta_{xy}) + C_y^2 (\sigma_{yy}^{\text{NS}} + \Delta_{yy}) + \frac{1}{2\lambda} (\sigma_{zz}^{\text{NS}} + \Delta_{zz})) \right. \\ \left. + \frac{4\lambda}{5p} (C_x (q_x^{\text{NS}} + \Delta_x) + C_y (q_y^{\text{NS}} + \Delta_y)) \left[\lambda (C_x^2 + C_y^2 + \frac{1}{2\lambda}) - \frac{5}{2} \right] \right\}, \quad (52)$$

$$b^{\text{modified}} = b^{\text{eq}} \left\{ 1 + \frac{\lambda}{p} (C_x^2 (\sigma_{xx}^{\text{NS}} + \Delta_{xx}) + 2C_x C_y (\sigma_{xy}^{\text{NS}} + \Delta_{xy}) + C_y^2 (\sigma_{yy}^{\text{NS}} + \Delta_{yy}) + \frac{3}{2\lambda} (\sigma_{zz}^{\text{NS}} + \Delta_{zz})) \right. \\ \left. + \frac{4\lambda}{5p} (C_x (q_x^{\text{NS}} + \Delta_x) + C_y (q_y^{\text{NS}} + \Delta_y)) \left[\lambda (C_x^2 + C_y^2 + \frac{3}{2\lambda}) - \frac{5}{2} \right] \right\}. \quad (53)$$

Until now, we establish a modified form to approximate initial gas distribution function by introducing the additional correction terms to the stress tensor and heat flux. In this work, we will not seek to find explicit forms to compute the correction terms. Instead, we will present an iterative procedure to update them. This will be addressed in the following section.

IV. GAS KINETIC FLUX SOLVER FOR FLOWS BEYOND NS LEVEL

In the previous section, a modified form is proposed for approximation of initial gas distribution function for flows beyond the NS level. This modified form will be used to compute the distribution function at the cell interface, which will be further utilized to evaluate numerical fluxes in the GKFS. By substituting Eq. (52) into Eq. (28) and Eq. (53) into Eq. (29), the modified gas distribution function at the cell interface can be formulated as

$$h^{\text{modified}}(\mathbf{x}_f, \mathbf{u}, t + \delta t) = \frac{\tau}{\tau + \delta t} h^{\text{modified}}(\mathbf{x}_f - \mathbf{u}\delta t, \mathbf{u}, t) \\ + \frac{\delta t}{\tau + \delta t} h^{\text{eq}}(\mathbf{x}_f, \mathbf{u}, t + \delta t), \quad (54)$$

$$b^{\text{modified}}(\mathbf{x}_f, \mathbf{u}, t + \delta t) = \frac{\tau}{\tau + \delta t} b^{\text{modified}}(\mathbf{x}_f - \mathbf{u}\delta t, \mathbf{u}, t) \\ + \frac{\delta t}{\tau + \delta t} b^{\text{eq}}(\mathbf{x}_f, \mathbf{u}, t + \delta t). \quad (55)$$

In the following, we will show the details of GKFS for evaluation of numerical fluxes. The first step will be the calculation of initial gas distribution function at the surrounding points of the cell interface.

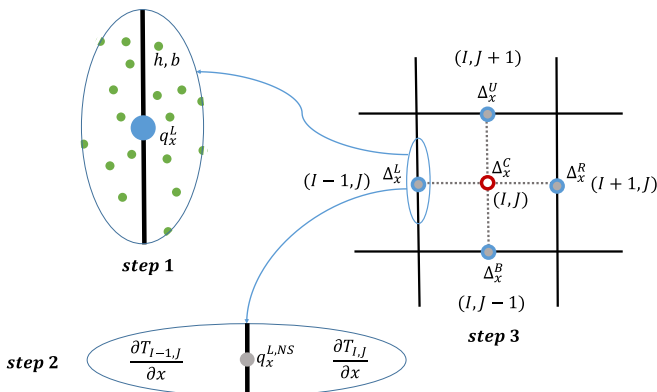


FIG. 1. The schematic of calculating the correction terms.

A. Reconstruction of distribution function at surrounding points of cell interface

For simplicity, we assume that two neighboring cells I and $I + 1$ are along the x direction. The initial gas distribution function $h^{\text{modified}}(\mathbf{x}_f - \mathbf{u}\delta t, \mathbf{u}, t)$ at the neighboring points of cell interface \mathbf{x}_f can be calculated by

$$h^{\text{modified}}(\mathbf{x}_f - \mathbf{u}\delta t, \mathbf{u}, t) \\ = \begin{cases} h_L^{\text{modified}}(\mathbf{x}_f, \mathbf{u}, t) - \nabla h^{\text{modified}}(\mathbf{x}_I, \mathbf{u}, t) \cdot \mathbf{u}\delta t, & u > 0 \\ h_R^{\text{modified}}(\mathbf{x}_f, \mathbf{u}, t) - \nabla h^{\text{modified}}(\mathbf{x}_{I+1}, \mathbf{u}, t) \cdot \mathbf{u}\delta t, & u < 0 \end{cases} \quad (56)$$

where \mathbf{x}_I represents the central position of cell I , which is at the left side of cell interface \mathbf{x}_f , and \mathbf{x}_{I+1} means the central position of cell $I + 1$, which is at the right side of cell interface \mathbf{x}_f . $\bullet L$ and $\bullet R$ are the values of h^{modified} at the left and the right sides of the interface, respectively. $\nabla h^{\text{modified}}$ is the gradient of the distribution function h^{modified} and it can be calculated by the central difference scheme. Taking the x direction as an example, on the uniform mesh, we have

$$\frac{\partial h^{\text{modified}}(\mathbf{x}_I, \mathbf{u}, t)}{\partial x} = \frac{h^{\text{modified}}(\mathbf{x}_{I+1}, \mathbf{u}, t) - h^{\text{modified}}(\mathbf{x}_{I-1}, \mathbf{u}, t)}{2 \cdot \delta x}, \quad (57)$$

where δx is the mesh spacing in the x direction. $h^{\text{modified}}(\mathbf{x}_{I+1}, \mathbf{u}, t)$ and $h^{\text{modified}}(\mathbf{x}_{I-1}, \mathbf{u}, t)$ are the distribution functions at the centers of cell $I + 1$ and cell $I - 1$, respectively. The distribution functions at the left and the right sides of the interface are interpolated from the distribution functions

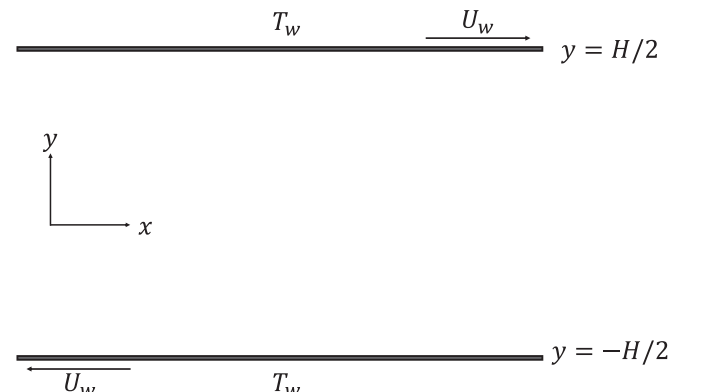
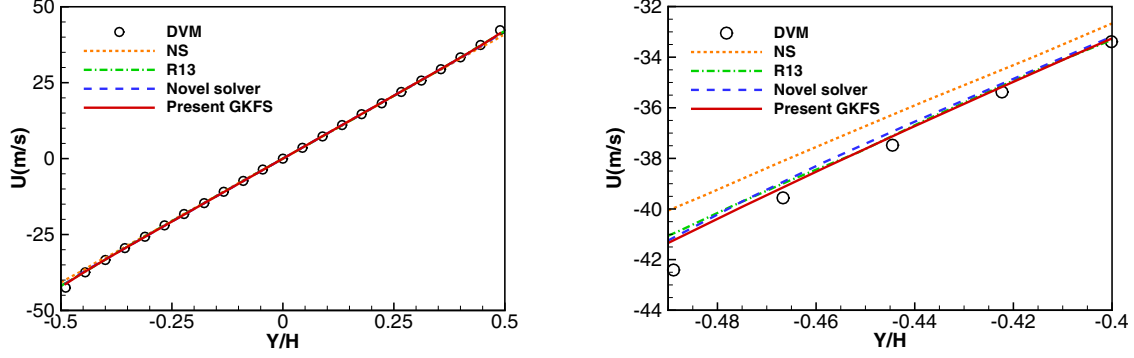


FIG. 2. The schematic of planar Couette flow.


 FIG. 3. Comparison of velocity profiles (left) and enlarged ones (right) for $\text{Kn} = 0.1$.

at cell centers as

$$h_L^{\text{modified}}(\mathbf{x}_f, \mathbf{u}, t) = h^{\text{modified}}(\mathbf{x}_I, \mathbf{u}, t) + \frac{\partial h^{\text{modified}}(\mathbf{x}_I, \mathbf{u}, t)}{\partial x} \cdot (\mathbf{x}_f - \mathbf{x}_I), \quad (58)$$

$$h_R^{\text{modified}}(\mathbf{x}_f, \mathbf{u}, t) = h^{\text{modified}}(\mathbf{x}_{I+1}, \mathbf{u}, t) + \frac{\partial h^{\text{modified}}(\mathbf{x}_{I+1}, \mathbf{u}, t)}{\partial x} \cdot (\mathbf{x}_f - \mathbf{x}_{I+1}). \quad (59)$$

The initial gas distribution function $b^{\text{modified}}(\mathbf{x}_f - \mathbf{u}\delta t, \mathbf{u}, t)$ at the surrounding point of \mathbf{x}_f can be calculated by adopting exactly the same approach.

B. Determination of equilibrium distribution function at cell interface

Once the initial distribution function at the surrounding point is approximated, our next task is to determine the equilibrium distribution function at the cell interface. As shown in Eq. (5) and Eq. (6), the distribution function at equilibrium state at the cell interface \mathbf{x}_f is merely relevant to the macroscopic variables $\mathbf{W}_f = (\rho, \rho U, \rho V, \rho E)_f^T$. Hence, the construction of double-distribution functions $h^{\text{eq}}(\mathbf{x}_f, \mathbf{u}, t + \delta t)$ and $b^{\text{eq}}(\mathbf{x}_f, \mathbf{u}, t + \delta t)$ is equivalent to the

calculation of mass, momentum, and energy at the cell interface. Since \mathbf{W}_f are conserved during the collision process, h and h^{eq} satisfy the conservation constraint at any time and space. Hence, at the time step $t + \delta t$ and interface \mathbf{x}_f , we have

$$\langle h(\mathbf{x}_f, \mathbf{u}, t + \delta t) - h^{\text{eq}}(\mathbf{x}_f, \mathbf{u}, t + \delta t) \rangle = 0, \quad (60)$$

$$\langle \mathbf{u}h(\mathbf{x}_f, \mathbf{u}, t + \delta t) - \mathbf{u}h^{\text{eq}}(\mathbf{x}_f, \mathbf{u}, t + \delta t) \rangle = 0, \quad (61)$$

$$\langle \mathbf{v}h(\mathbf{x}_f, \mathbf{u}, t + \delta t) - \mathbf{v}h^{\text{eq}}(\mathbf{x}_f, \mathbf{u}, t + \delta t) \rangle = 0, \quad (62)$$

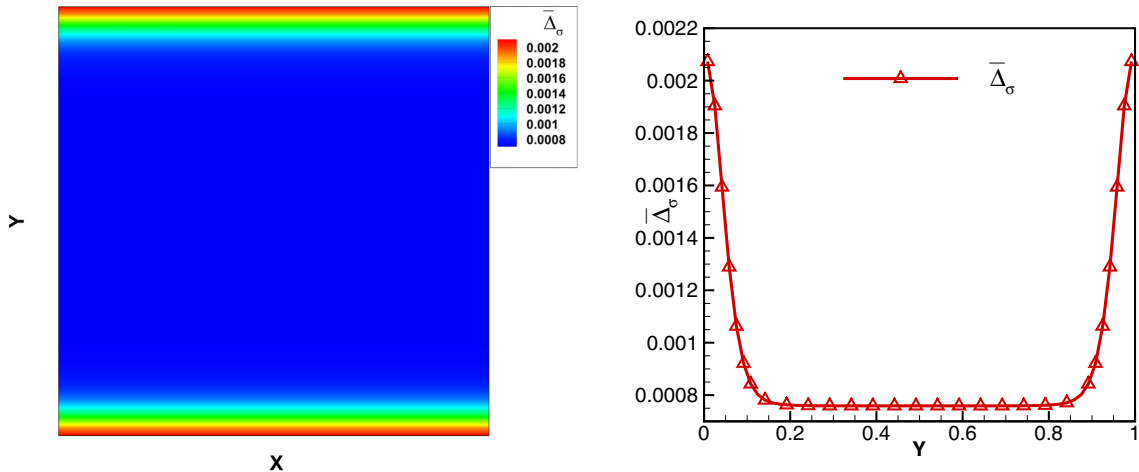
$$\frac{1}{2} \langle \mathbf{u}^2 [h(\mathbf{x}_f, \mathbf{u}, t + \delta t) - h^{\text{eq}}(\mathbf{x}_f, \mathbf{u}, t + \delta t)] + b(\mathbf{x}_f, \mathbf{u}, t + \delta t) - b^{\text{eq}}(\mathbf{x}_f, \mathbf{u}, t + \delta t) \rangle = 0. \quad (63)$$

Substituting the expression of $h(\mathbf{x}_f, \mathbf{u}, t + \delta t)$ and $b(\mathbf{x}_f, \mathbf{u}, t + \delta t)$ given in Eqs. (28) and (29) into Eqs. (60)–(63) and with the help of moment relationship shown in Eqs.(11)–(14), the above equations can be reformulated into

$$\rho_f = \langle h^{\text{eq}}(\mathbf{x}_f, \mathbf{u}, t + \delta t) \rangle = \langle h(\mathbf{x}_f - \mathbf{u}\delta t, \mathbf{u}, t) \rangle, \quad (64)$$

$$(\rho \mathbf{U})_f = \langle \mathbf{u}h^{\text{eq}}(\mathbf{x}_f, \mathbf{u}, t + \delta t) \rangle = \langle \mathbf{u}h(\mathbf{x}_f - \mathbf{u}\delta t, \mathbf{u}, t) \rangle, \quad (65)$$

$$(\rho E)_f = \frac{1}{2} \langle \mathbf{u}^2 h^{\text{eq}}(\mathbf{x}_f - \mathbf{u}\delta t, \mathbf{u}, t) + b^{\text{eq}}(\mathbf{x}_f - \mathbf{u}\delta t, \mathbf{u}, t) \rangle = \frac{1}{2} \langle \mathbf{u}^2 h(\mathbf{x}_f - \mathbf{u}\delta t, \mathbf{u}, t) + b(\mathbf{x}_f - \mathbf{u}\delta t, \mathbf{u}, t) \rangle. \quad (66)$$


 FIG. 4. The contour of $\bar{\Delta}_\sigma$ (left) and its value along vertical central line (right) for $\text{Kn} = 0.1$.

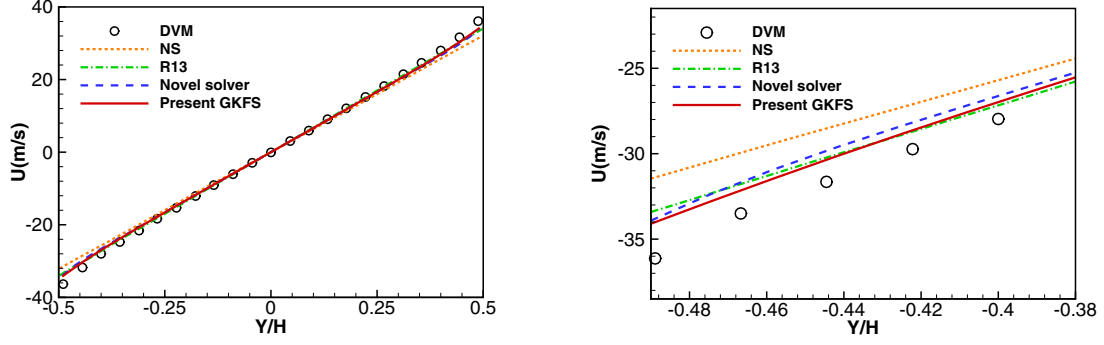


FIG. 5. Comparison of velocity profiles (left) and enlarged ones (right) for $Kn = 0.25$.

By substituting the initial distribution function at the surrounding point into Eqs. (64)–(66), the conservative flow variables \mathbf{W}_f at the cell interface \mathbf{x}_f can be calculated by

$$\rho_f = \int h^{\text{modified}}(\mathbf{x}_f - \mathbf{u}\delta t, \mathbf{u}, t) d\mathbf{u}, \quad (67)$$

$$(\rho \mathbf{U})_f = \int \mathbf{u} h^{\text{modified}}(\mathbf{x}_f - \mathbf{u}\delta t, \mathbf{u}, t) d\mathbf{u}, \quad (68)$$

$$(\rho E)_f = \frac{1}{2} \int [\mathbf{u}^2 h^{\text{modified}}(\mathbf{x}_f - \mathbf{u}\delta t, \mathbf{u}, t) + b^{\text{modified}}(\mathbf{x}_f - \mathbf{u}\delta t, \mathbf{u}, t)] d\mathbf{u}. \quad (69)$$

Once the conservative variables are all known, the double-equilibrium distribution functions $h^{\text{eq}}(\mathbf{x}_f, \mathbf{u}, t)$, $b^{\text{eq}}(\mathbf{x}_f, \mathbf{u}, t)$ and relaxation time τ_f at the cell interface could be constructed accordingly.

C. Update of correction terms for stress tensor and heat flux

As discussed in Sec. III, introducing correction terms to stress tensor and heat flux in approximation of initial gas distribution function is the key for simulation of flows beyond NS level. It will be tedious to derive relevant differential equations to compute these correction terms. On the other hand, we notice that for general rarefied flows, the stress tensor and

heat flux can be calculated from the moment integrals of distribution function. This means that at the cell interface, once the distribution function is obtained, the actual stress tensor and heat flux can be calculated. In the meantime, the stress tensor and heat flux in the NS level can be computed from the velocity and temperature gradients by using Eqs. (39)–(44). The difference between them is actually the correction term. This principle forms a foundation to design an iterative process to update the correction terms. In the simulation, the initial values of correction terms are all set as zero. After that, the update of correction terms is made by a procedure with three steps. The schematic of this procedure is shown in Fig. 1, and the three steps are described below.

1. Step 1: Calculate the stress tensor and heat flux at the cell interface from the distribution function

According to the moment relationship, the stress tensors σ_{ij} and heat fluxes q_i are all related to the gas distribution function. Taking the heat flux in the x direction as an example, we have

$$q_x = \frac{1}{2} \langle C_x [(C_x^2 + C_y^2)h + b] \rangle. \quad (70)$$

By substituting the expression of the distribution functions at the cell interface calculated in Eq. (54) and Eq. (55) into the above equation, heat flux at the left cell interface could be

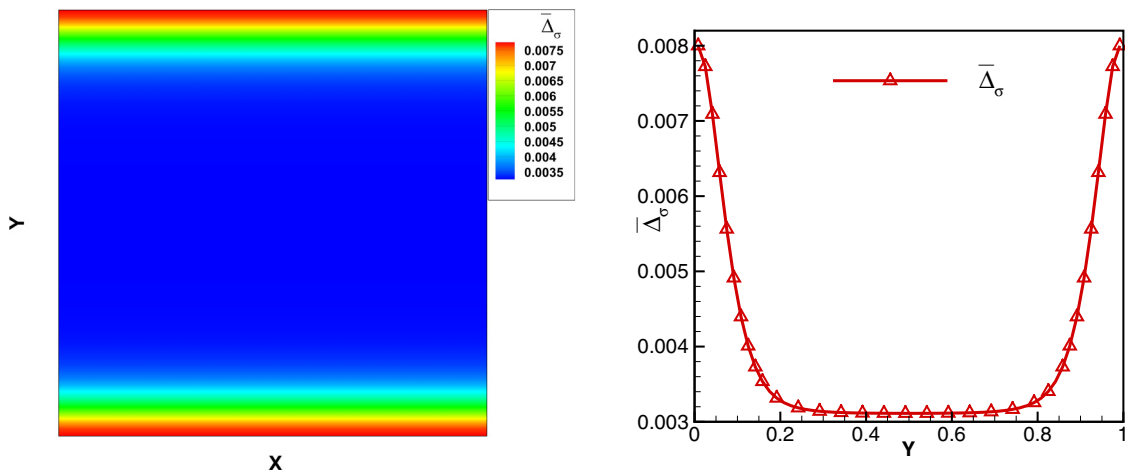
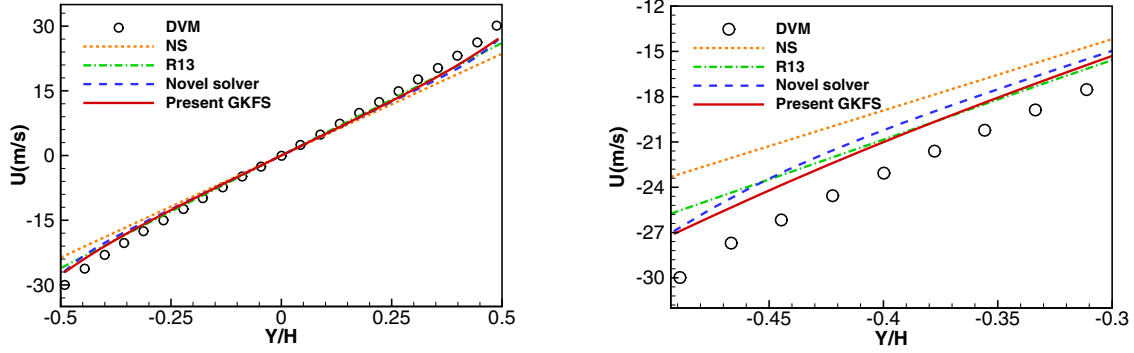


FIG. 6. The contour of $\bar{\Delta}_\sigma$ (left) and its value along vertical central line (right) for $Kn = 0.25$.


 FIG. 7. Comparison of velocity profiles (left) and enlarged ones (right) for $\text{Kn} = 0.5$.

calculated by

$$q_x^L = \frac{1}{2} \langle C_x [(C_x^2 + C_y^2) \cdot h(\mathbf{x}_f, \mathbf{u}, t + \delta t) + b(\mathbf{x}_f, \mathbf{u}, t + \delta t)] \rangle. \quad (71)$$

Using the same way, the stress tensor σ_{ij}^L and heat flux q_y^L at the left interface could also be calculated. Their moment relations are listed as follows:

$$\sigma_{xx} = \frac{1}{3} \langle (2C_x^2 - C_y^2) h - b \rangle, \quad (72)$$

$$\sigma_{xy} = \langle C_x C_y h \rangle, \quad (73)$$

$$\sigma_{yy} = \frac{1}{3} \langle (2C_y^2 - C_x^2) h - b \rangle, \quad (74)$$

$$\sigma_{zz} = -\sigma_{xx} - \sigma_{yy}, \quad (75)$$

$$q_y = \frac{1}{2} \langle C_y [(C_x^2 + C_y^2) h + b] \rangle. \quad (76)$$

2. Step 2: Compute the stress tensor and heat flux at the cell interface in the NS level

In the NS level, the stress tensor can be computed from the linearized constitutive relationship and the heat flux can be calculated from Fourier's law. They are related to the velocity and temperature gradients, which can be approximated by the central difference scheme. Taking the heat flux $q_x^{L,NS}$ in the x direction as an example, it can be calculated by averaging the spatial derivatives of temperature at the centers of cell

$(I-1, J)$ and (I, J) . Hence, $q_x^{L,NS}$ can be calculated by

$$q_x^{L,NS} = -\frac{5\mu}{4\lambda T} \left(\frac{\partial T_{I-1,J}/\partial x + \partial T_{I,J}/\partial x}{2} \right). \quad (77)$$

The other NS stress tensor and heat flux could be computed using the same way.

3. Step 3: Update the correction terms at the cell center

For the left interface, the correction terms are calculated by comparing the difference between actual stress tensor–heat flux and NS stress tensor–heat flux. Taking the correction term Δ_x^L as an example, it is calculated by

$$\Delta_x^L = q_x^L - q_x^{L,NS}. \quad (78)$$

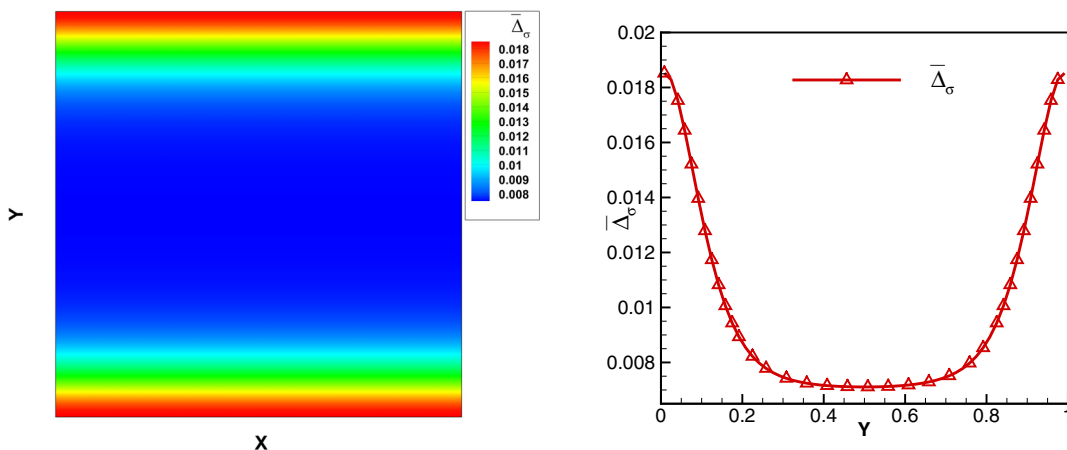
The other correction terms for heat flux in the x direction on the right, upper, and bottom interfaces of the cell (I, J) can be calculated in the same way as

$$\Delta_x^R = q_x^R - q_x^{R,NS}, \quad (79)$$

$$\Delta_x^U = q_x^U - q_x^{U,NS}, \quad (80)$$

$$\Delta_x^B = q_x^B - q_x^{B,NS}. \quad (81)$$

Finally, on the uniform mesh, the correction terms at the cell center could be evaluated by averaging the values at four


 FIG. 8. The contour of $\bar{\Delta}_\sigma$ (left) and its value along vertical central line (right) for $\text{Kn} = 0.5$.

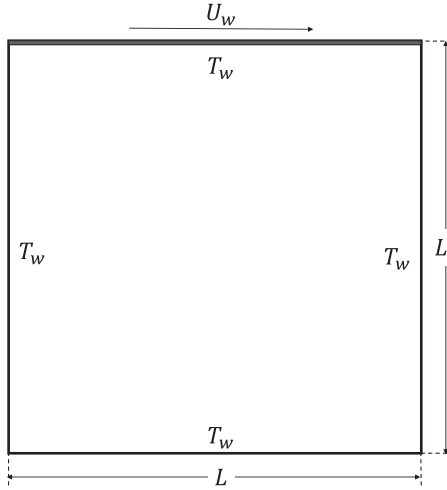


FIG. 9. Schematic of lid-driven cavity flow.

cell interfaces as

$$\Delta_x^C = \frac{\Delta_x^L + \Delta_x^R + \Delta_x^U + \Delta_x^B}{4}. \quad (82)$$

The other correction terms at the cell center, such as Δ_{xx}^C , Δ_{xy}^C , Δ_{yy}^C , and Δ_y^C , can be updated following the three steps

shown above. For Δ_{yx}^C and Δ_{zz}^C , their values can be given out directly by

$$\Delta_{yx}^C = \Delta_{xy}^C, \quad (83)$$

$$\Delta_{zz}^C = -\Delta_{xx}^C - \Delta_{yy}^C. \quad (84)$$

D. Numerical approximation of integrals

In GKFS, the computation of macroscopic variables, flux vector, and correction terms is based on the moment integration of distribution function in the particle velocity space. Theoretically, analytical forms of integrals for the modified gas distribution function can be given out. In this work, for simplicity, numerical quadrature is used for approximation of integrals. In the future work, analytical forms of integrals for this solver will be presented for saving computational effort.

For low-speed flows with small temperature variation, the high-order Gauss-Hermite quadrature rule [53,54] could be the best choice for approximation of integrals. For a function $h(u)$, the integral can be approximated as

$$\int_{-\infty}^{+\infty} h(u) du = \int_{-\infty}^{+\infty} e^{-u^2} [e^{u^2} h(u)] du \approx \sum_{\alpha=1}^Q w_{\alpha} e^{u_{\alpha}^2} h(u_{\alpha}), \quad (85)$$

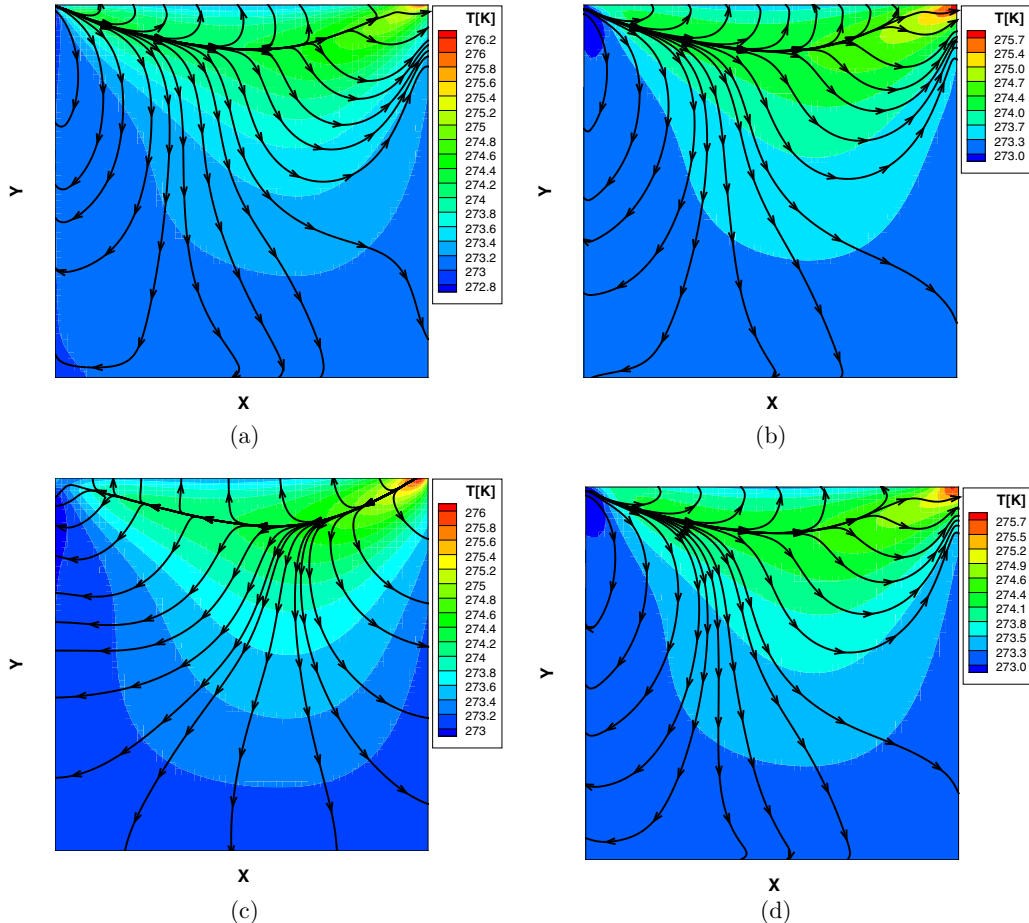


FIG. 10. The comparison of temperature contours and streamlines of heat flux by different approaches for $Kn = 0.01$: (a) DVM, (b) novel solver, (c) conventional GKFS, (d) present GKFS.

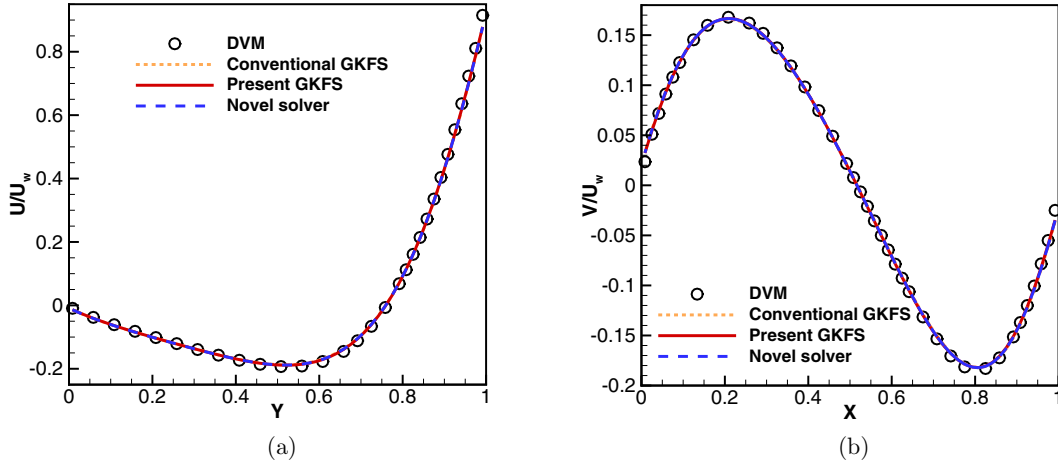


FIG. 11. Comparison of velocity profiles along central line for $Kn = 0.01$: (a) vertical U -velocity profiles, (b) horizontal V -velocity profiles.

where e^{-u^2} is the weighting function and w_α is the corresponding quadrature weight, which can be calculated by

$$w_\alpha = \frac{2^{Q-1} Q! \sqrt{\pi}}{Q^2 [H_{Q-1}(u_\alpha)]^2}. \quad (86)$$

Here, $H_Q(u)$ is the Q th Gauss-Hermite polynomial and $u_\alpha (\alpha = 1, \dots, Q)$ are the positive roots of $H_Q(u)$. To apply the numerical quadrature rule, $\mathbf{u}_\alpha = (u_q, v_p)$ are used to discretize the particle velocity space $\mathbf{u} = (u, v)$, where $q = 1, \dots, Q_x$ and $p = 1, \dots, Q_y$ are indices to represent the velocity point (q, p) . By applying the integral quadrature, the conservative variables $\mathbf{W}_f = (\rho, \rho U, \rho V, \rho E)_f$ at the cell interface can be approximately calculated by

$$\rho_f \approx \sum_{\alpha} w_{\alpha} h^{\text{modified}}(\mathbf{x}_f - \mathbf{u}_{\alpha} \delta t, \mathbf{u}_{\alpha}, t), \quad (87)$$

$$(\rho U)_f \approx \sum_{\alpha} w_{\alpha} u_{\alpha} h^{\text{modified}}(\mathbf{x}_f - \mathbf{u}_{\alpha} \delta t, \mathbf{u}_{\alpha}, t), \quad (88)$$

$$(\rho E)_f \approx \frac{1}{2} \sum_{\alpha} w_{\alpha} [u_{\alpha}^2 h^{\text{modified}}(\mathbf{x}_f - \mathbf{u}_{\alpha} \delta t, \mathbf{u}_{\alpha}, t) + b^{\text{modified}}(\mathbf{x}_f - \mathbf{u}_{\alpha} \delta t, \mathbf{u}_{\alpha}, t)]. \quad (89)$$

Here, $h^{\text{modified}}(\mathbf{x}_f - \mathbf{u}_{\alpha} \delta t, \mathbf{u}_{\alpha}, t)$ and $b^{\text{modified}}(\mathbf{x}_f - \mathbf{u}_{\alpha} \delta t, \mathbf{u}_{\alpha}, t)$ are the modified initial distribution functions

at the surrounding points of cell interface \mathbf{x}_f . Similarly, numerical fluxes in the x direction at the cell interface can be approximately computed by

$$F_{\rho}^x \approx \sum_{\alpha} w_{\alpha} u_{\alpha} h^{\text{modified}}(\mathbf{x}_f, \mathbf{u}_{\alpha}, t), \quad (90)$$

$$F_{\rho U}^x \approx \sum_{\alpha} w_{\alpha} u_{\alpha} u_{\alpha} h^{\text{modified}}(\mathbf{x}_f, \mathbf{u}_{\alpha}, t), \quad (91)$$

$$F_{\rho E}^x \approx \frac{1}{2} \sum_{\alpha} w_{\alpha} u_{\alpha} [u_{\alpha}^2 h^{\text{modified}}(\mathbf{x}_f, \mathbf{u}_{\alpha}, t) + b^{\text{modified}}(\mathbf{x}_f, \mathbf{u}_{\alpha}, t)]. \quad (92)$$

The stress tensor and heat flux at the cell interface can be rewritten in the form of numerical quadrature as

$$\sigma_{xx} \approx \frac{1}{3} \sum_{\alpha} w_{\alpha} [(2C_{x,\alpha}^2 - C_{y,\alpha}^2) \cdot h^{\text{modified}}(\mathbf{x}_f, \mathbf{u}_{\alpha}, t) - b^{\text{modified}}(\mathbf{x}_f, \mathbf{u}_{\alpha}, t)] \quad (93)$$

$$\sigma_{xy} \approx \sum_{\alpha} w_{\alpha} C_{x,\alpha} C_{y,\alpha} \cdot h^{\text{modified}}(\mathbf{x}_f, \mathbf{u}_{\alpha}, t), \quad (94)$$

$$\sigma_{yy} \approx \frac{1}{3} \sum_{\alpha} w_{\alpha} [(2C_{y,\alpha}^2 - C_{x,\alpha}^2) \cdot h^{\text{modified}}(\mathbf{x}_f, \mathbf{u}_{\alpha}, t) - b^{\text{modified}}(\mathbf{x}_f, \mathbf{u}_{\alpha}, t)], \quad (95)$$

$$\sigma_{zz} = -\sigma_{xx} - \sigma_{yy}, \quad (96)$$

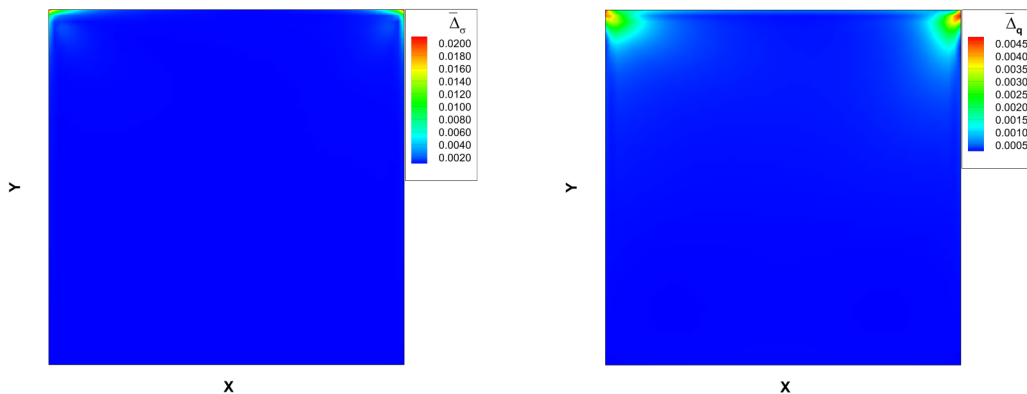


FIG. 12. The contours of $\bar{\Delta}_\sigma$ and $\bar{\Delta}_q$ for $Kn = 0.01$.

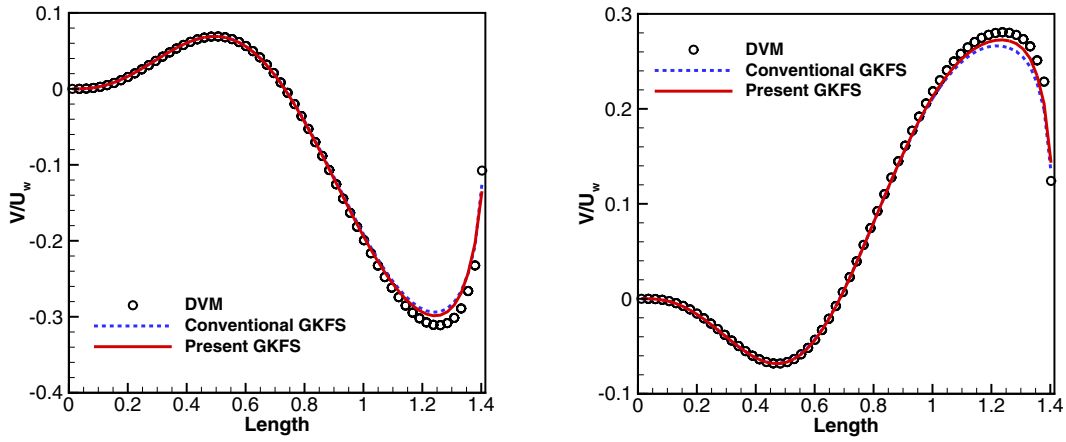


FIG. 13. Comparison of velocity profiles along the diagonal lines for Kn = 0.01.

$$q_x \approx \frac{1}{2} \sum_{\alpha} w_{\alpha} C_{x,\alpha} [(C_{x,\alpha}^2 + C_{y,\alpha}^2) \cdot h^{\text{modified}}(\mathbf{x}_f, \mathbf{u}_{\alpha}, t) + b^{\text{modified}}(\mathbf{x}_f, \mathbf{u}_{\alpha}, t)], \tag{97}$$

$$q_y \approx \frac{1}{2} \sum_{\alpha} w_{\alpha} C_{y,\alpha} [(C_{x,\alpha}^2 + C_{y,\alpha}^2) \cdot h^{\text{modified}}(\mathbf{x}_f, \mathbf{u}_{\alpha}, t) + b^{\text{modified}}(\mathbf{x}_f, \mathbf{u}_{\alpha}, t)]. \tag{98}$$

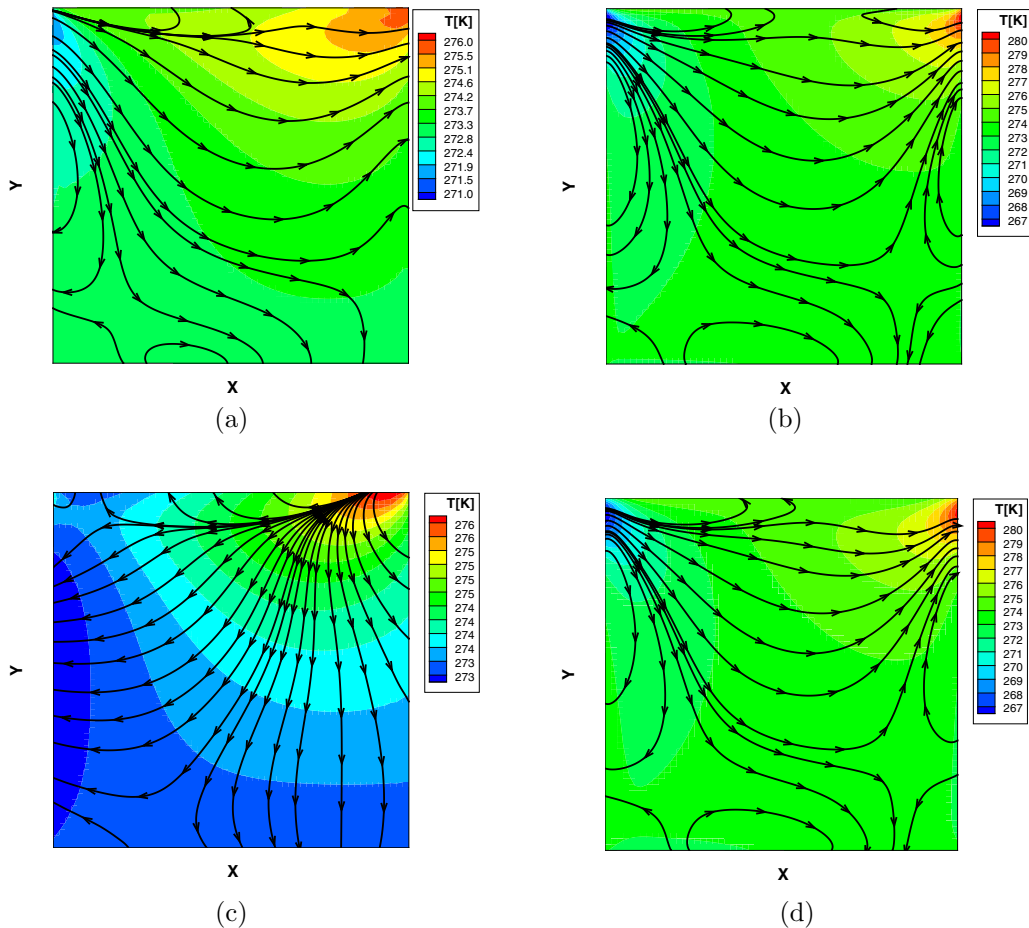


FIG. 14. The comparison of temperature contours and streamlines of heat flux by different approaches for Kn = 0.0798: (a) DVM, (b) novel solver, (c) conventional GKFS, (d) present GKFS.

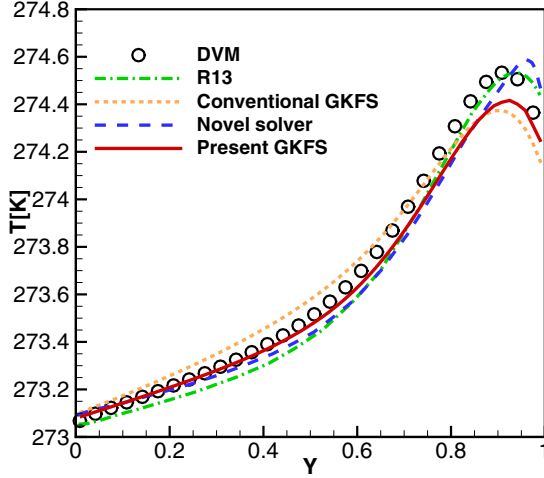


FIG. 15. Comparison of temperature profiles along vertical central line for $\text{Kn} = 0.0798$.

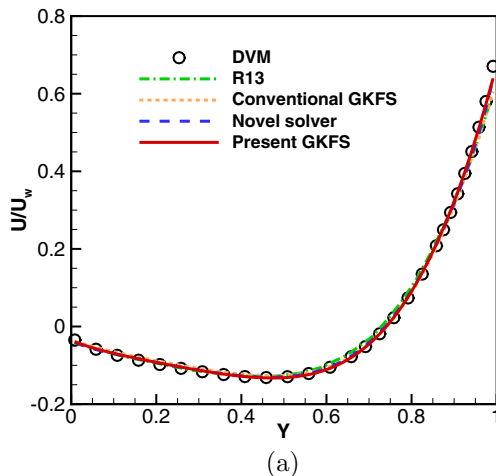
E. Implementation of kinetic boundary conditions

To evaluate numerical fluxes at the boundary, the distribution function at the wall should be determined first. In this work, the isothermal wall boundary condition is considered. According to no-penetration condition, we can have the following relationship:

$$\sum_{\alpha} w_{\alpha} u_{\alpha} h^{\text{out}}(\mathbf{x}_w, \mathbf{u}_{\alpha}, t) H(A) + \sum_{\alpha} w_{\alpha} u_{\alpha} h^{\text{in}}(\mathbf{x}_w, \mathbf{u}_{\alpha}, t) [1 - H(A)] = 0, \quad (99)$$

where \mathbf{x}_w denotes the midpoint of a cell interface on the wall; h^{out} represents the distribution function reflected from the wall surface. h^{in} denotes the incident distribution function in the flow domain. $A = \mathbf{u}_{\alpha} \cdot \mathbf{n}_w$, where \mathbf{n}_w stands for the outward unit vector normal to the wall surface and $H[A]$ is the Heaviside function defined as

$$H[A] = \begin{cases} 0, & A < 0 \\ 1, & A > 0 \end{cases}. \quad (100)$$



Based on the Maxwellian boundary condition with perfect thermalizing wall [55], the particle is recognized leaving with the equilibrium state because of the frequent interaction with the boundary. Then, the distribution function reflected from the wall can be given as

$$h^{\text{out}}(\mathbf{x}_w, \mathbf{u}_{\alpha}, t) = \frac{\rho_w \lambda_w}{\pi} e^{-\lambda_w [(\mathbf{u}_{\alpha} - \mathbf{U}_w)^2]}. \quad (101)$$

Here, $\lambda_w = 1/2RT_w$, T_w is the wall temperature, and \mathbf{U}_w means the wall velocity vector. ρ_w is the density on the wall, which will be determined from the no-penetration condition. The $h^{\text{in}}(\mathbf{x}_w, \mathbf{u}_{\alpha}, t)$ in the flow domain around the wall is considered as $h^{\text{modified}}(\mathbf{x}_w - \mathbf{u}_{\alpha} \delta t, \mathbf{u}_{\alpha}, t)$. By substituting the expression of $h^{\text{in}}(\mathbf{x}_w, \mathbf{u}_{\alpha}, t)$ and $h^{\text{out}}(\mathbf{x}_w, \mathbf{u}_{\alpha}, t)$ into Eq. (99), the density at the wall surface can be calculated as [56]

$$\rho_w = - \frac{\sum_{\alpha} w_{\alpha} u_{\alpha} h^{\text{in}}(\mathbf{x}_w, \mathbf{u}_{\alpha}, t) [1 - H(A)]}{\frac{\lambda_w}{\pi} \sum_{\alpha} w_{\alpha} u_{\alpha} e^{-\lambda_w [(\mathbf{u}_{\alpha} - \mathbf{U}_w)^2]} H(A)}. \quad (102)$$

Finally, the distribution function at the surrounding points of the wall surface can be expressed as

$$h(\mathbf{x}_w - \mathbf{u}_{\alpha} \delta t, \mathbf{u}_{\alpha}, t) = h^{\text{out}}(\mathbf{x}_w, \mathbf{u}_{\alpha}, t) H(A) + h^{\text{in}}(\mathbf{x}_w, \mathbf{u}_{\alpha}, t) [1 - H(A)]. \quad (103)$$

The same expression holds for $b(\mathbf{x}_w - \mathbf{u}_{\alpha} \delta t, \mathbf{u}_{\alpha}, t)$. Once the gas distribution function around the wall is obtained, the conservative variables on the wall can be calculated by Eqs. (87)–(89). Then, the numerical fluxes at the wall can be calculated by Eqs. (90)–(92).

F. Time discretization

After evaluation of flux vector \mathbf{F} at each cell interface, the discrete Eq. (25) becomes a set of ordinary differential equations, which can be solved by the third-order total variation diminishing Runge-Kutta method [57,58] due to its lower consumption of storage [14]. At first, Eq. (25) is rewritten as

$$\frac{d\mathbf{W}}{dt} = \mathbf{L}(\mathbf{W}), \quad (104)$$

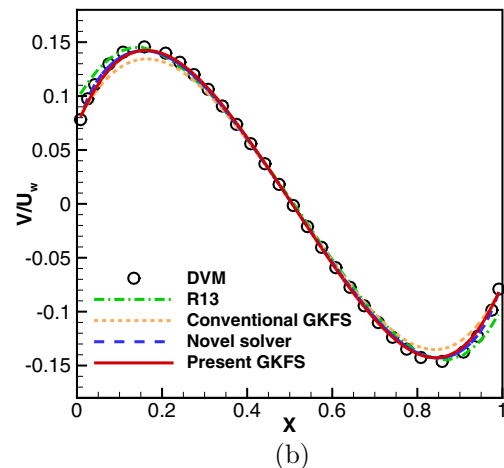
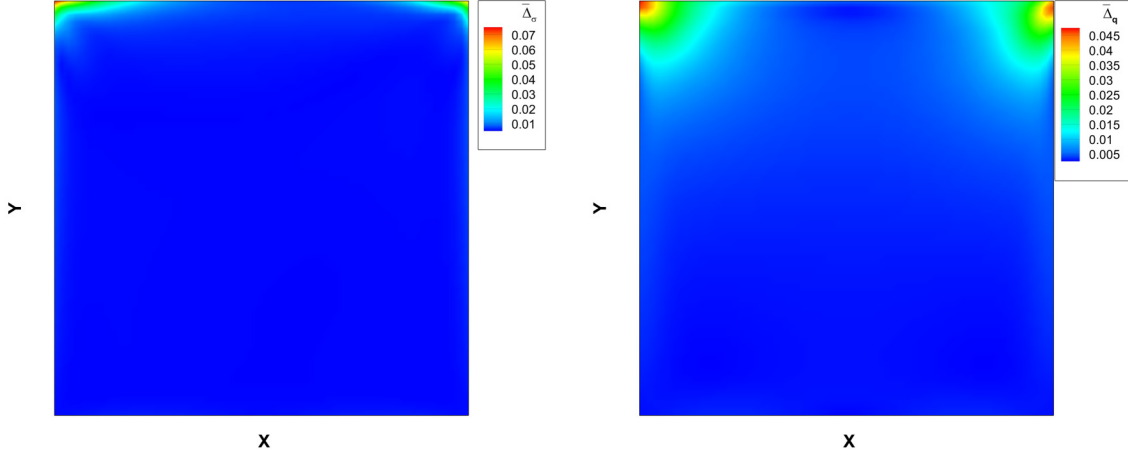


FIG. 16. Comparison of velocity profiles along central line for $\text{Kn} = 0.0798$: (a) vertical U -velocity profiles, (b) horizontal V -velocity profiles.

FIG. 17. The contours of $\bar{\Delta}_\sigma$ and $\bar{\Delta}_q$ for $\text{Kn} = 0.0798$.

with $\mathbf{L}(\mathbf{W}) = -\frac{1}{\Omega} \sum_{n=1}^N \mathbf{F}_n S_n$. Then, time discretization is implemented as

$$\begin{aligned} \mathbf{W}^{(0)} &= \mathbf{W}^n \\ \mathbf{W}^{(1)} &= \mathbf{W}^{(0)} + \mathbf{L}(\mathbf{W}^{(0)})\Delta t \\ \mathbf{W}^{(2)} &= \frac{3}{4}\mathbf{W}^{(0)} + \frac{1}{4}\mathbf{W}^{(1)} + \frac{1}{4}\mathbf{L}(\mathbf{W}^{(1)})\Delta t \\ \mathbf{W}^{(3)} &= \frac{1}{3}\mathbf{W}^{(0)} + \frac{2}{3}\mathbf{W}^{(2)} + \frac{2}{3}\mathbf{L}(\mathbf{W}^{(2)})\Delta t \\ \mathbf{W}^{n+1} &= \mathbf{W}^{(3)}, \end{aligned} \quad (105)$$

where Δt is the marching time step for the evolution of the macroscopic flow variables. In the present solver, the time step Δt is determined by the CFL condition,

$$\Delta t = \text{CFL} \frac{\min\{\delta\mathbf{x}\}}{\max\{|\mathbf{u}_\alpha|\}}, \quad (106)$$

where CFL represents the CFL number. $\delta\mathbf{x} = (\delta x, \delta y)$ is the grid spacing in x and y direction. $\max\{|\mathbf{u}_\alpha|\}$ means the maximum discrete particle velocity. In addition, the streaming time step δt for the local solution reconstruction at the cell interface should be specified. The main constraint here is to restrict the local reconstructing points within the neighboring cells. To

satisfy this criterion, it can be computed by

$$\delta t < \frac{\min\{\delta\mathbf{x}\}}{2 \max\{|\mathbf{u}_\alpha|\}}. \quad (107)$$

G. Computational procedure

For illustration purpose, the basic computational procedure of present solver is summarized as follows:

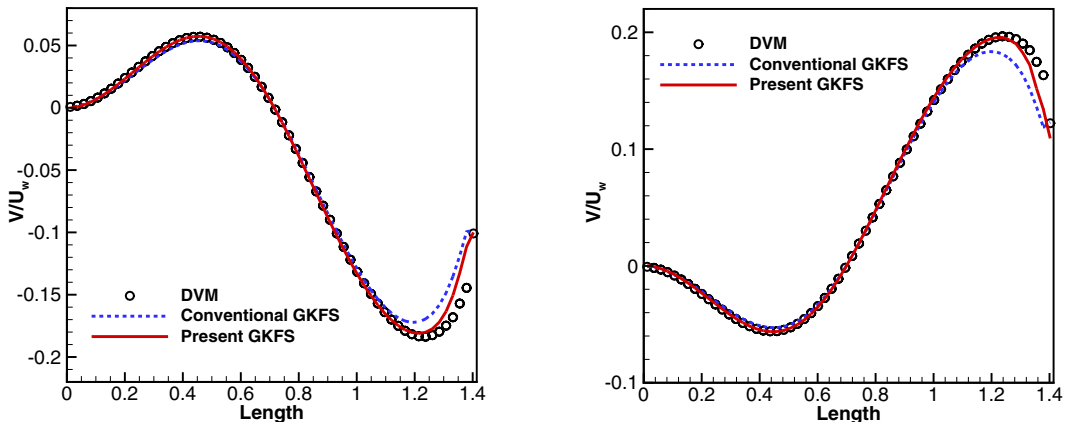
(i) Initialization: Discretize the physical and particle velocity spaces by \mathbf{x}_i and \mathbf{u}_α , respectively. Predict the time step Δt and streaming time step δt by Eq. (106) and Eq. (107).

(ii) Reconstruct the initial distribution functions $h^{\text{modified}}(\mathbf{x}_f - \mathbf{u}\delta t, t)$ with Eq. (56). Then, compute $b^{\text{modified}}(\mathbf{x}_f - \mathbf{u}\delta t, t)$ in the same way.

(iii) Calculate the conservative variables \mathbf{W}_f at cell interface using Eqs. (87)–(89). Then, reconstruct the distribution function $h^{\text{eq}}(\mathbf{x}_f, \mathbf{u}, t)$ and $b^{\text{eq}}(\mathbf{x}_f, \mathbf{u}, t)$ at equilibrium state by Eq. (5) and Eq. (6).

(iv) Construct the distribution functions $h(\mathbf{x}_f, \mathbf{u}, t)$ and $b(\mathbf{x}_f, \mathbf{u}, t)$ at cell interface using Eq. (54) and Eq. (55).

(v) Implement the boundary condition: density ρ_w at the boundary point is firstly computed by Eq. (102), and the distribution functions $h(\mathbf{x}_w - \mathbf{u}_\alpha\delta t, \mathbf{u}_\alpha, t)$ are then obtained with Eq. (103). After that, take the same procedure to calculate $b(\mathbf{x}_w - \mathbf{u}_\alpha\delta t, \mathbf{u}_\alpha, t)$.

FIG. 18. Comparison of velocity profiles along the diagonal lines for $\text{Kn} = 0.0798$.

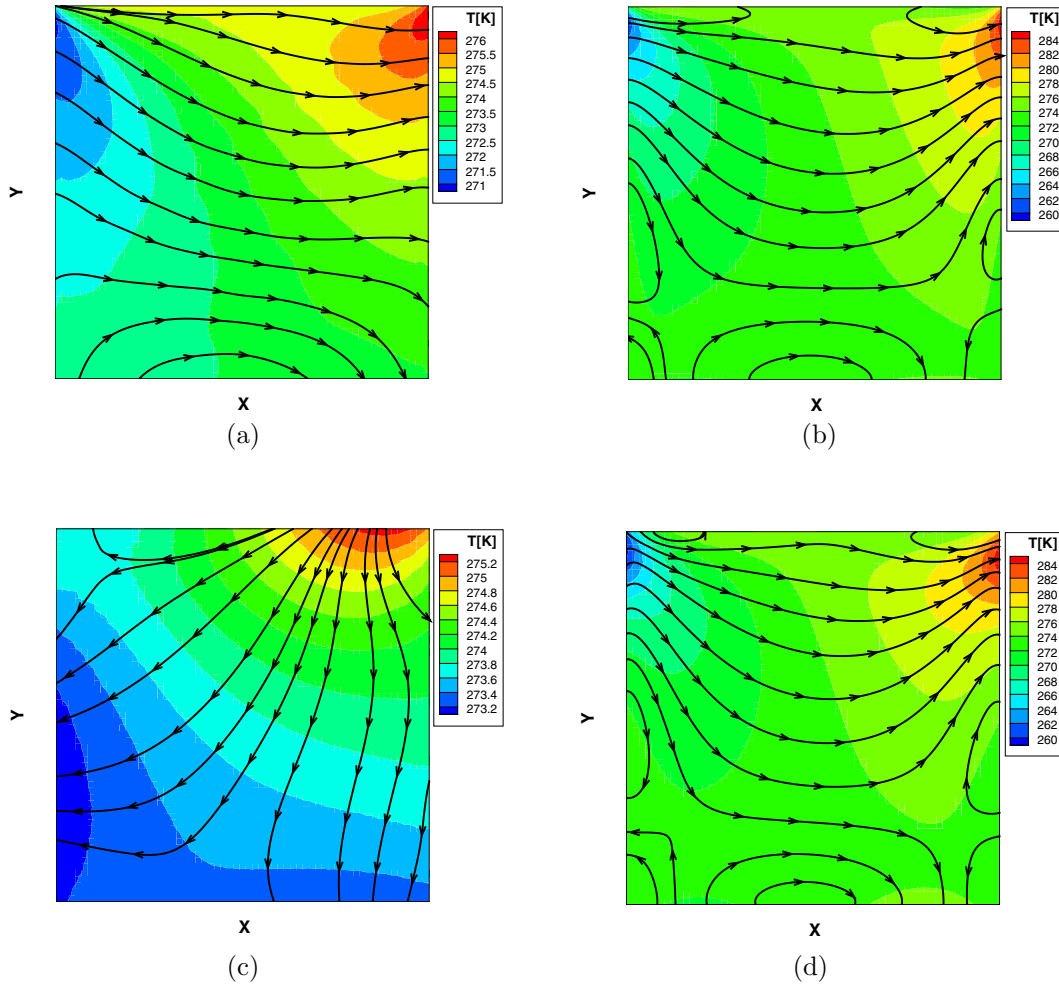


FIG. 19. The comparison of temperature contours and streamlines of heat flux by different approaches for $Kn = 0.3989$: (a) DVM, (b) novel solver, (c) conventional GKFS, (d) present GKFS.

(vi) Adopt Eqs. (90)–(92) to evaluate the numerical flux $\mathbf{F}^x = (F_\rho^x, F_{\rho U}^x, F_{\rho V}^x, F_{\rho E}^x)^T$ at the cell interface. Calculate the numerical flux \mathbf{F}^y in a similar way.

(vii) Update the correction terms Δ_{ij} and Δ_i in the modified gas distribution as shown in Sec. IV C.

(viii) Use three-stage Runge-Kutta scheme shown in Eq. (105) to update the macroscopic variables at cell centers.

(ix) Repeat steps (ii)–(viii) until the whole computation satisfies the convergence criterion.

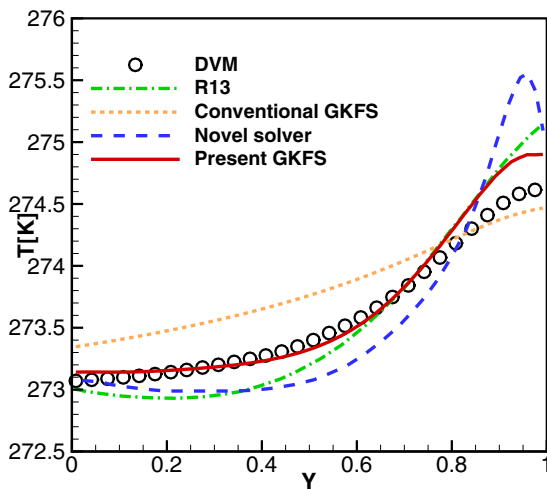


FIG. 20. Comparison of temperature profiles along vertical central line for $Kn = 0.3989$.

V. NUMERICAL EXAMPLES

In this section, the proposed new variant of GKFS is validated by simulating flows from the continuum regime to the transition regime. Comparison of numerical results from various solvers is made for test cases of planar Couette flow, lid-driven cavity flow, and bottom-heated square cavity. As discussed in Sec. III, the correction terms for stress tensor and heat flux are the key for simulation of flows beyond NS level. To visualize the high-order correction terms in the flow field, herein we define two parameters $\bar{\Delta}_\sigma$ and $\bar{\Delta}_q$ as follows:

$$\bar{\Delta}_\sigma = \sqrt{\sum (\Delta_{ij}^2)}, \tag{108}$$

$$\bar{\Delta}_q = \sqrt{\sum (\Delta_i^2)}. \tag{109}$$

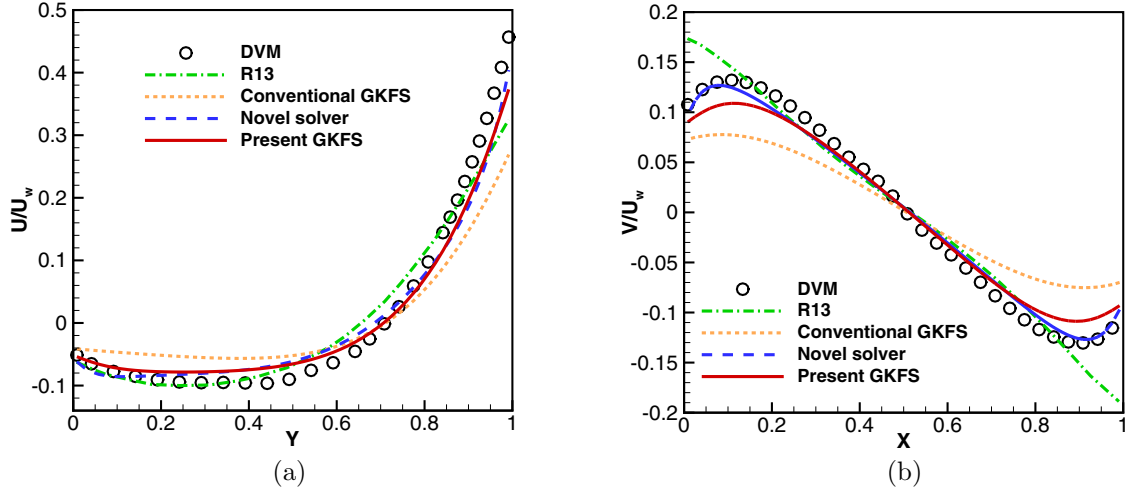


FIG. 21. Comparison of velocity profiles along central line for $Kn = 0.3989$: (a) vertical U -velocity profiles, (b) horizontal V -velocity profiles.

A. Case 1: Planar Couette flow

At first, the planar Couette flow for argon gas in the transition regime is simulated to validate the present solver. This case has been simulated by Gu and Emerson [20] using the NS equations and R13 equations. Liu *et al.* [33] also tested this problem by adopting discrete velocity method (DVM) and a novel solver. As known, the velocity profile for planar Couette flow is linear in the continuum regime, and it will be nonlinear in the near-surface region when it comes to the rarefied regime. This is a critical rarefaction phenomenon known as the Knudsen layer or kinetic boundary layer [45]. Hence, it is a good example for us to test the performance of present solver for planar Couette flow in the transition regime.

As shown in Fig. 2, two parallel plates are set at $y = \pm H/2$, and velocity of the upper and lower moving walls is set as $U_w = \pm 50$ m/s. The wall temperature is fixed at $T_w = 273$ K. The left and right boundaries are both set with the periodic boundary condition. Computational domain is divided uniformly into 60×60 cells for all cases. In the particle velocity space, the Gauss-Hermite rule with eight quadrature points is adopted for integral quadrature.

In the simulation, the viscosity is obtained from Sutherland’s law:

$$\mu = \mu_{\text{ref}} \left(\frac{T}{T_{\text{ref}}} \right)^{1.5} \frac{T_{\text{ref}} + T_s}{T + T_s}, \quad (110)$$

where $T_{\text{ref}} = 273$ (K), $T_s = 104$ (K). The Knudsen number is defined as $Kn = \lambda/H$, where λ is the mean-free path of molecule and can be related to the reference viscosity by

$$\lambda = \frac{\mu_{\text{ref}}}{p} \sqrt{\frac{\pi RT_{\text{ref}}}{2}}. \quad (111)$$

According to the definition of Knudsen number, the reference viscosity can be expressed by

$$\mu_{\text{ref}} = KnHp \sqrt{\frac{2}{\pi RT_{\text{ref}}}}. \quad (112)$$

In the present work, three benchmark cases with Knudsen numbers of 0.1, 0.25, and 0.5 are considered. Figure 3 shows the comparison of velocity profiles obtained by different approaches at the upper limit of slip regime with $Kn = 0.1$. As

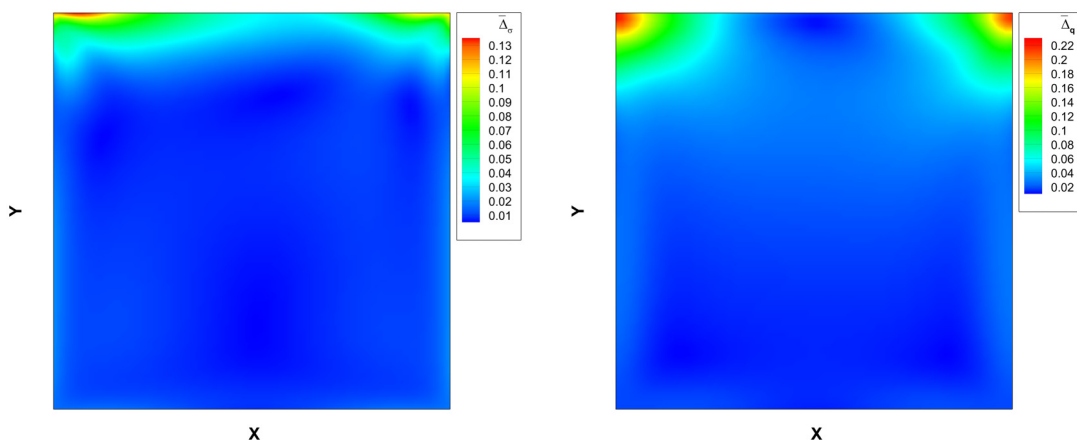


FIG. 22. The contours of $\bar{\Delta}_\alpha$ and $\bar{\Delta}_q$ for $Kn = 0.3989$.

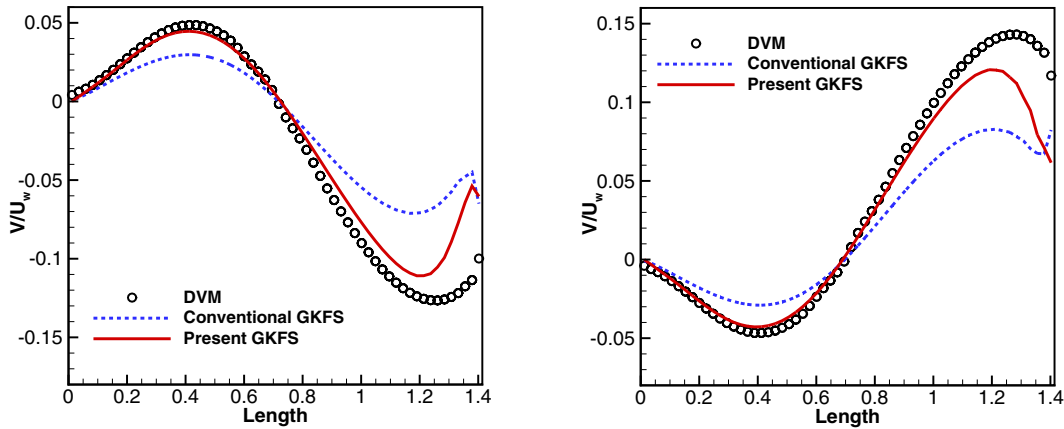


FIG. 23. Comparison of velocity profiles along the diagonal lines for $Kn = 0.3989$.

shown in the enlarged plot of Fig. 3, the NS solver could capture the wall-slip phenomenon near the moving plates; however, the value of wall slip is overpredicted. In contrast, the result of present GKFS is comparable with that from novel solver or R13 equations and even much closer to the result of DVM. We hold the view that the better prediction of velocity profiles is mainly related to the correction terms to the stress tensor. To further validate this standpoint, the contour of $\bar{\Delta}_\sigma$, which is defined in Eq. (108), is displayed in Fig. 4. It is apparent to see that the correction terms for stress tensor mainly take effect in the near-surface region and its peak value is equal to 0.002. Therefore, the correction term within the Knudsen layer indeed contributes to the better prediction of velocity profile. Additionally, the values of $\bar{\Delta}_\sigma$ in the central part of the Couette flow are relatively small. Hence, $\bar{\Delta}_\sigma$ almost makes no contribution to the correction of linearized stress tensor in the central equilibrium region.

As seen in Fig. 5, when the Knudsen number is increased to the early transition regime with $Kn = 0.25$, the nonlinear effect within the Knudsen layer increases simultaneously. From the enlarged plot of Fig. 5, we can see that NS equations and R13 equations both fail to capture the nonlinear

Knudsen layer effect. In contrast, the new variant of GKFS can basically predict the power-law behavior of the velocity profile and agrees better with the DVM data than the novel solver. Figure 6 illustrates the contour of $\bar{\Delta}_\sigma$ and its value along the vertical central line. It is noted that the correction term to stress tensor indeed makes sense within the Knudsen layer and its peak value is increased to 0.008. For the central equilibrium part, the values are still relatively small, which means the correction terms almost take no effect in the central region.

As illustrated in Fig. 7, at $Kn = 0.5$, which is in the transition regime, there exists extremely strong rarefaction effect in the near-surface region. The DVM data shows the expected nonlinear velocity profiles. Although both NS and R13 solvers fail to capture this aspect of velocity profile, the results from the present solver follow this behavior and capture the slip at the wall in better agreement with DVM than the novel solver. As seen in Fig. 8, the correction terms to the stress tensor take more effect with the increase of Knudsen number. The peak value of $\bar{\Delta}_\sigma$ inside the Knudsen layer has been increased to 0.0185. Based on the results shown above, we may conclude that it is the merit of additional correction terms that enable

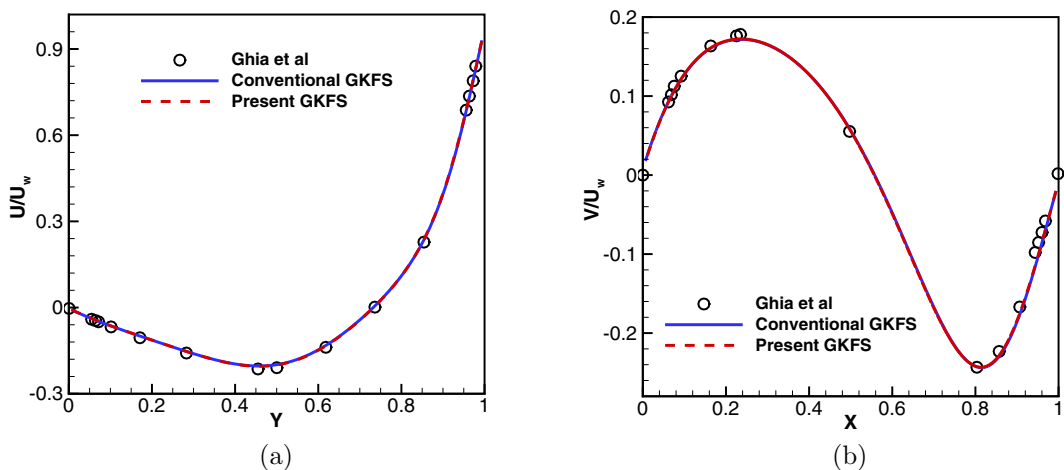


FIG. 24. Comparison of velocity profiles along central line for $Re = 100$: (a) vertical U -velocity profiles, (b) horizontal V -velocity profiles.

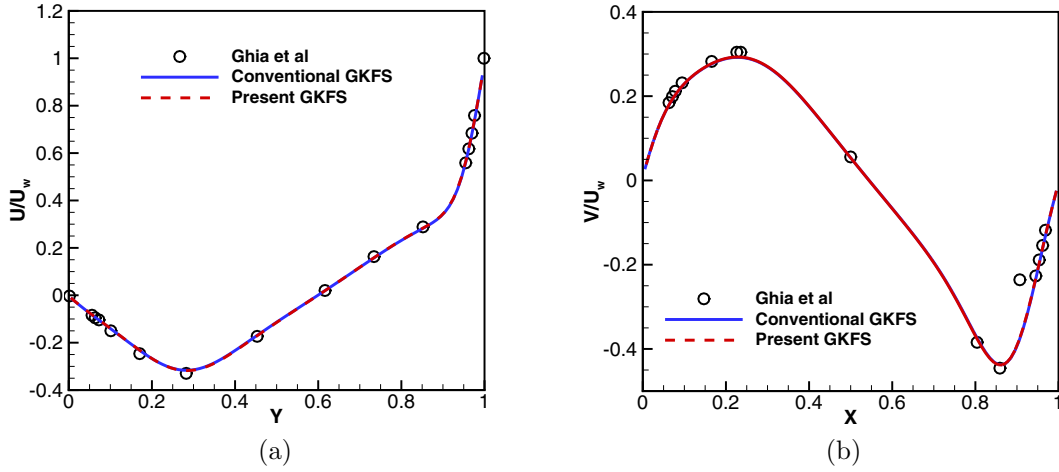


FIG. 25. Comparison of velocity profiles along central line for $Re = 400$: (a) vertical U -velocity profiles, (b) horizontal V -velocity profiles.

the new variant of GKFS to have the capability for prediction of strong nonequilibrium effect in the Knudsen layer.

B. Case 2: Lid-driven cavity flows

The second test case is the 2D lid-driven cavity flow. This case has been researched by Rana *et al.* [59] using R13 equations, and Liu *et al.* [33] using the novel solver. The schematic of lid-driven cavity flow is shown in Fig. 9. The velocity of upper boundary is $U_w = 50$ m/s and wall temperature T_w is set as 273 K.

In the simulation, the viscosity μ is given by the inverse power law

$$\mu = \mu_{ref} \left(\frac{T}{T_{ref}} \right)^\omega, \quad (113)$$

where the reference temperature is $T_{ref} = 273$ K and the exponent is $\omega = 1$. The mean-free path λ is related to the reference viscosity by

$$\lambda = \frac{\mu_{ref}}{\rho_{ref} \sqrt{RT_{ref}}}, \quad (114)$$

in which ρ_{ref} is the reference density. Based on the definition of Knudsen number, $Kn = \lambda/L$, the reference viscosity can be expressed by

$$\mu_{ref} = KnL\rho_{ref}\sqrt{RT_{ref}}. \quad (115)$$

Here, the monatomic rarefied gas with $Kn = 0.01, 0.0798,$ and 0.3989 is considered, and the present results are compared with those from other solvers such as DVM, novel solver, and conventional GKFS. The computational domain is divided uniformly into 60×60 cells and the Gauss-Hermite quadrature with 8×8 points is adopted. It is noteworthy that for the simulation by DVM, the Gauss-Hermite quadrature with 28×28 points is utilized to ensure the convergence.

In Fig. 10, we compare the temperature contours and the streamlines of heat flux. We can see that the heat flux predicted by DVM, novel solver, and present GKFS all go from left upper corner to right upper corner (low-temperature region to high-temperature region). However, for conventional GKFS, this anti-Fourier heat transfer phenomenon cannot be captured. Figure 11 shows that velocity profiles along central line

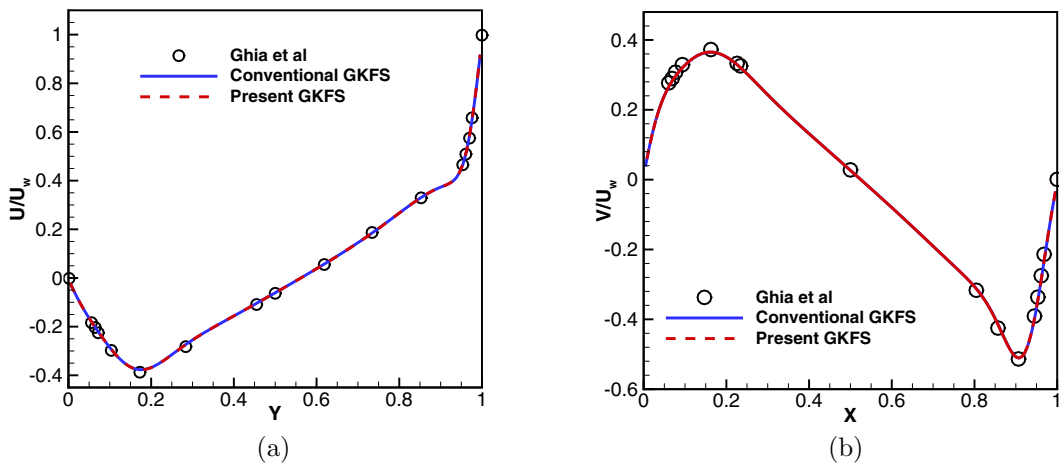


FIG. 26. Comparison of velocity profiles along central line for $Re = 1000$: (a) vertical U -velocity profiles, (b) horizontal V -velocity profiles.

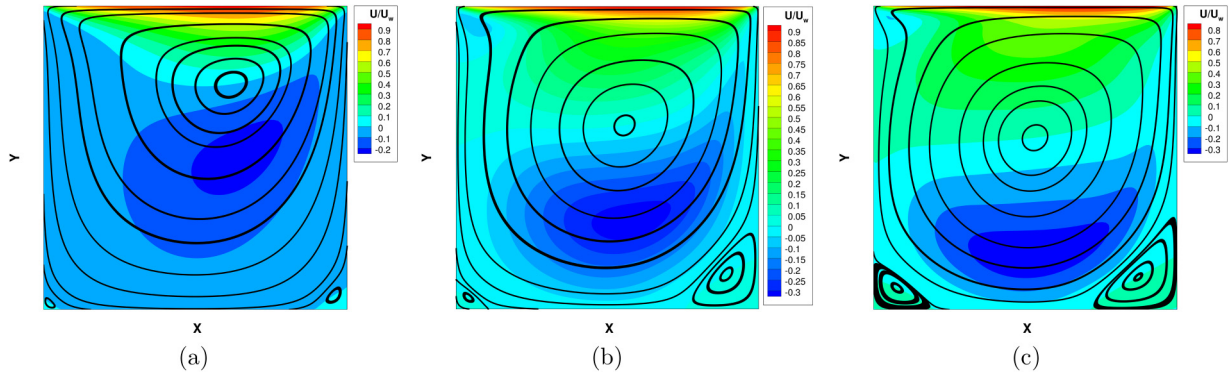


FIG. 27. The U -velocity contour and streamlines for different Reynolds numbers: (a) $Re = 100$, (b) $Re = 400$, (c) $Re = 1000$.

calculated by the four solvers match well with each other at $Kn = 0.01$.

To further explore the contribution of correction terms on the nonequilibrium region, the contours of $\bar{\Delta}_\sigma$ and $\bar{\Delta}_q$ for $Kn = 0.01$ are displayed in Fig. 12. It is obvious to see that the correction terms to stress tensor and heat flux are both mainly to take effect in the upper region of the left and right corners. To make the comparison in more detail, the velocity profiles obtained by conventional GKFS and present GKFS along the diagonal lines are compared in Fig. 13. The results suggest that the velocity profiles along the diagonal lines predicted by present GKFS match better with those of DVM results than conventional GKFS, especially near the region of the left and right corners. This provides clear evidence that the correction terms really take effect near the region of the left and right corners.

As shown in Fig. 14, the anti-Fourier heat transfer phenomenon can also be captured by DVM and novel solver for $Kn = 0.0798$. The most notable difference between conventional GKFS and present GKFS is the reversed direction of heat flux. For conventional GKFS, Fourier’s law forces the heat flux vector pointing from hot region to cold region. However, in the present GKFS, the direction is inverted and heat is transferred from cold region to hot region. The comparison of temperature profiles along the vertical central line is illustrated in Fig. 15. As we can see, the temperature deviates only slightly from the wall temperature because the frictional heating is quite weak. The results predicted by present GKFS agree better with the DVM data than conventional GKFS,

especially in the bottom region of cavity. However, it underpredicts the temperature near the moving wall.

Figure 16 shows the U -velocity and V -velocity profiles along vertical and horizontal centerline. For the V -velocity distribution, the result given by R13 equations slightly deviates from DVM near the wall boundary. Conventional GKFS slightly underpredicts the peak value of V velocity. The present GKFS and novel solver both predict the data as well as DVM. The contours of $\bar{\Delta}_\sigma$ and $\bar{\Delta}_q$ for $Kn = 0.0798$ are demonstrated in Fig. 17. Compared with the contours shown in Fig. 12, it appears that the correction terms to stress tensor and heat flux enlarge with the increasing of Knudsen number. In Fig. 18, the velocity profiles along the diagonal lines are compared. The results show that the velocity profiles predicted by present GKFS are in better agreement with those of DVM results than conventional GKFS. Hence, it can be further deduced that the correction terms indeed make contribution in the strong nonequilibrium region of the flow field.

Figure 19 shows the comparison of temperature contour and heat flux lines obtained by different approaches for the larger Knudsen number with $Kn = 0.3989$. The present GKFS can still well predict the anti-Fourier heat transfer behavior as DVM or novel solver does. For conventional GKFS, the streamlines of heat flux still go from the high-temperature region to the low-temperature region as limited by the Fourier heat transfer law. In Fig. 20, we compare the temperature profiles along the vertical line across the center of cavity. The conventional GKFS overpredicts the temperature in the bottom region and underpredicts the temperature near

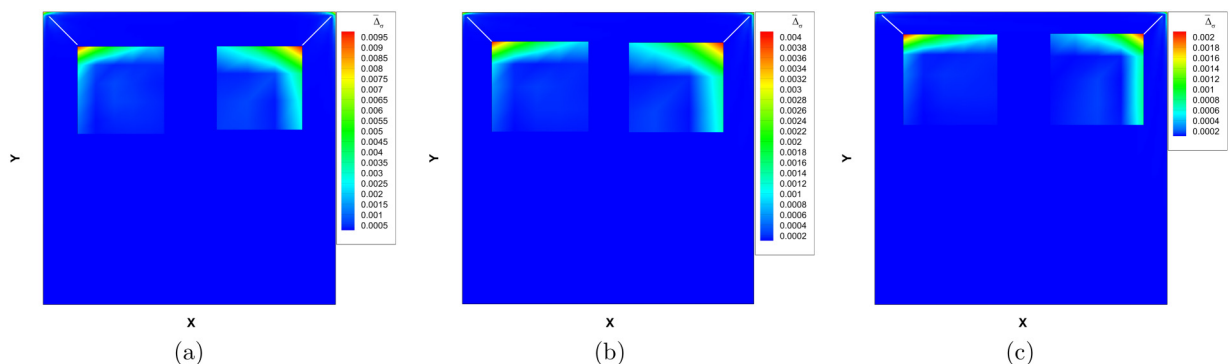


FIG. 28. The contours of $\bar{\Delta}_\sigma$ for flows in the continuum regime: (a) $Re = 100$, (b) $Re = 400$, (c) $Re = 1000$.

TABLE I. Locations of primary vortex centers obtained by different approaches.

Re	Ghia <i>et al.</i> [60]	Conventional GKFS	Present GKFS
100	(0.6172,0.7344)	(0.6181,0.7382)	(0.6175,0.7386)
400	(0.5547,0.6055)	(0.5563,0.6056)	(0.5560,0.6059)
1000	(0.5313,0.5625)	(0.5320,0.5653)	(0.5320,0.5654)

the wall boundary. In contrast, R13 solver, novel solver, and present GKFS show the opposite tendency. The present GKFS predicts the thermal behavior of the flow with reasonable accuracy compared with DVM data.

As displayed in Fig. 21, when the Knudsen number is increased to 0.3989, both U - and V -velocity profiles of different solvers start to deviate from the DVM data. Overall, the result of present GKFS is closer to DVM data as compared with conventional GKFS, which is attributed to the correction terms. However, it is noted that the peak value of V -velocity given by the novel solver is in better agreement with DVM than present GKFS. Figure 22 displays the contours of $\bar{\Delta}_\sigma$ and $\bar{\Delta}_q$ for $Kn = 0.3989$. Compared with the previous contours of correction terms at $Kn = 0.01$ and 0.0798 , the nonequilibrium region at $Kn = 0.3989$ is enlarged apparently. The correction terms contribute to the region not only in the upper corners but also near the whole moving boundary. From the comparison of velocity profiles along the diagonal lines shown in Fig. 23, we can conclude that the better performance of present GKFS than conventional GKFS is indeed attributed to the correction terms.

In addition, the simulation of continuum flows at Reynolds number of $Re = 100, 400,$ and 1000 are conducted to validate the present solver. The computational domain is divided uniformly into $80 \times 80, 100 \times 100,$ and 120×120 cells with the increase of Reynolds number. In these cases, the reference dynamic viscosity μ_{ref} is calculated by $\mu_{ref} = \rho_{ref} U_W L / Re$. As shown in Fig. 24, Fig. 25, and Fig. 26, the results of the present solver agree well with those of Ghia *et al.* [60] and the conventional GKFS. These test cases prove that the present solver can recover solutions of conventional GKFS in the continuum regime and give the same accurate results.

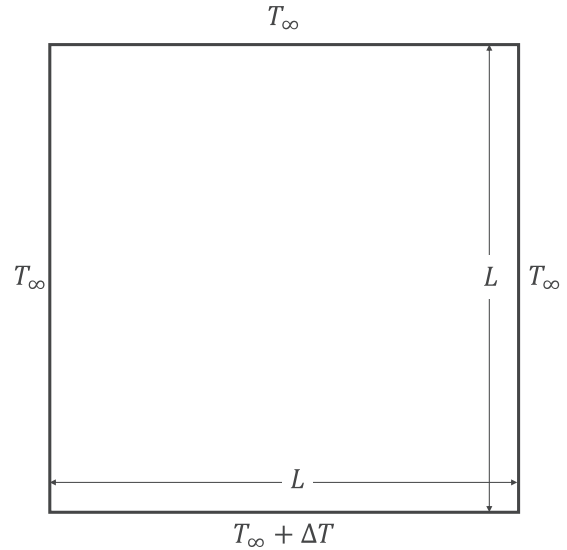


FIG. 30. The schematic of the problem.

As illustrated in Fig. 27, the present solver can capture two small eddies at the bottom corners reasonably. With the increasing of Reynolds number, vortex center moves towards the center of the cavity. Table I compares the locations of the primary vortex center with different Reynolds numbers obtained by conventional GKFS and present GKFS using eight quadrature points with those obtained by Ghia *et al.* [60]. As shown in this table, the maximum relative error between the present results and those of Ghia *et al.* [60] is less than 5.7%.

Figure 28 shows the contour of $\bar{\Delta}_\sigma$ for $Re = 100, 400,$ and 1000 in the continuum regime. It is noted that correction terms almost make no contribution in the whole flow field for the continuum flow, except a little contribution existing in the left and right corner of the moving wall. This implies that the present GKFS could recover solutions of NS equations in the continuum regime because the correction terms automatically take no effect for the flows in NS level.

At the same time, the effect of quadrature point number on the present solver is investigated. As shown in Fig. 29, the

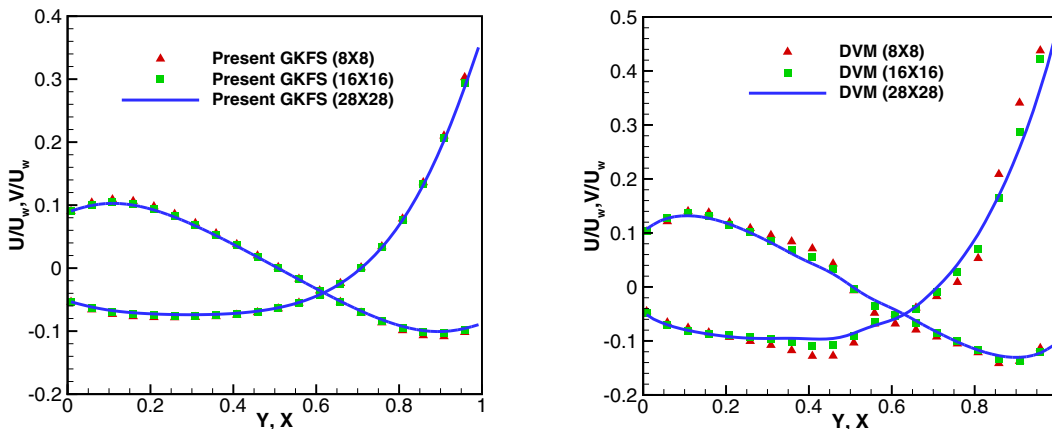


FIG. 29. The comparison of velocity profiles with different quadrature point numbers for present solver (left) and DVM (right) at $Kn = 0.3989$.

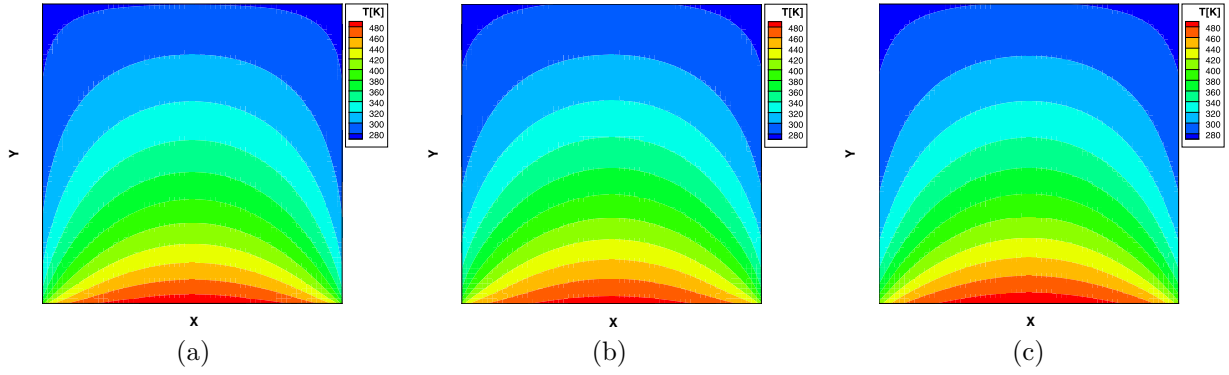


FIG. 31. Comparison of temperature contours by different solvers for $Kn = 0.05$: (a) DVM, (b) explicit novel solver, (c) present GKFS.

velocity profiles predicted by the present solver with 8×8 , 16×16 , and 28×28 quadrature points are the same. However, for the DVM method, the velocity profiles calculated with 8×8 and 16×16 quadrature points cannot converge to the results with 28×28 quadrature points. In this aspect, the present solver can adopt less quadrature points than DVM to obtain the converged results and thus improve the computational efficiency. Furthermore, the explicit formulations of the present gas distribution function shown in Eqs. (52) and (53), provide us an opportunity to derive the analytical forms in the future work. After that, the simulation efficiency can be further improved.

C. Case 3: Bottom-heated square cavity

For the previous two cases, the temperature difference is quite small and the present GKFS has shown potential for capturing the rarefaction effect. To further explore the ability of the present solver for flows with large temperature variation, we test the heat transfer flow in a bottom-heated square cavity [61]. The schematic diagram of this benchmark case is shown in Fig. 30. The temperature of the bottom wall is fixed at $T_\infty + \Delta T$, where T_∞ is the reference temperature and ΔT is the temperature difference. In the simulation, ΔT is considered as 300 K. For the other walls, their temperatures are kept at $T_\infty = 300$ K. In order to test the accuracy of the present solver for flows in the rarefied regime, the Knudsen

number is taken as 0.05 and 0.13. In Fig. 29, L is the length of the cavity and the computational domain is divided uniformly into 60×60 cells. In this case, the Gauss-Hermite quadrature points are increased to 28×28 for accurate description of gas distribution function. In the simulation, the viscosity μ is also calculated by Eq. (113). The mean-free path λ is determined by Eq. (114).

Figure 31 shows the comparison of temperature contours for $Kn = 0.05$ between DVM [62], explicit novel solver [34], and the present GKFS. The temperature profiles along the horizontal and vertical central line are displayed in Fig. 32. As seen in these two figures, the results of the present solver match well with those of DVM and the explicit novel solver. The comparison of temperature contours at $Kn = 0.13$ between DVM, explicit novel solver, and present solver is displayed in Fig. 33. As seen in Fig. 34, for the temperature profiles there exists a little difference between the present solver and DVM. As shown in Fig. 34(a), the horizontal temperature profile along the central line given by the present GKFS matches better with DVM than the explicit novel solver. On the other hand, for the vertical temperature profile, the explicit novel solver can give a slightly better result than present GKFS near the bottom wall. The contours of $\bar{\Delta}_q$ for $Kn = 0.05$ and $Kn = 0.13$ are shown in Fig. 35, which reveals that for flows arising from temperature difference, the nonequilibrium effect mainly occurs at the left and right corners of the heated wall.

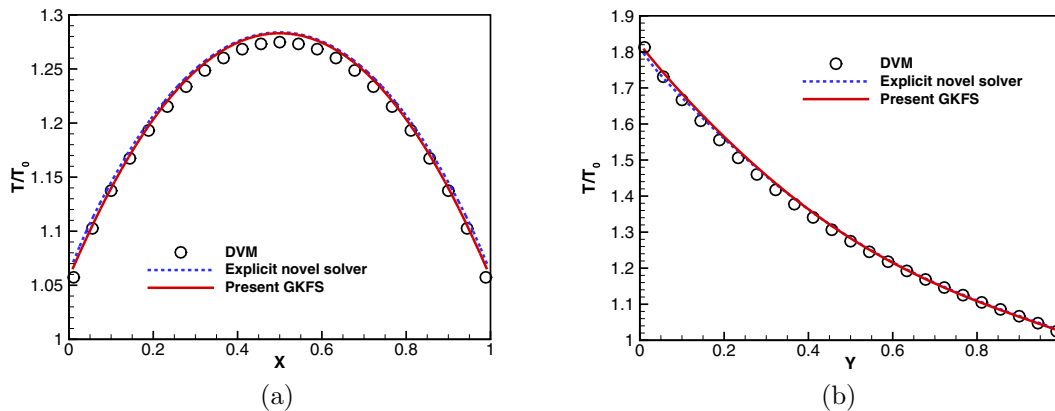


FIG. 32. Comparison of temperature profiles along central line for $Kn = 0.05$: (a) horizontal temperature profiles, (b) vertical temperature profiles.

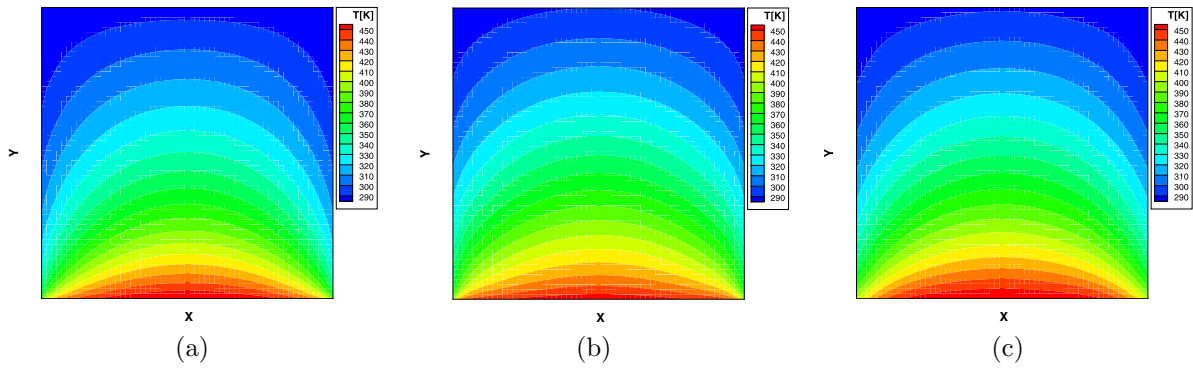


FIG. 33. Comparison of temperature contours by different solvers for $Kn = 0.13$: (a) DVM, (b) explicit novel solver, (c) present GKFS.

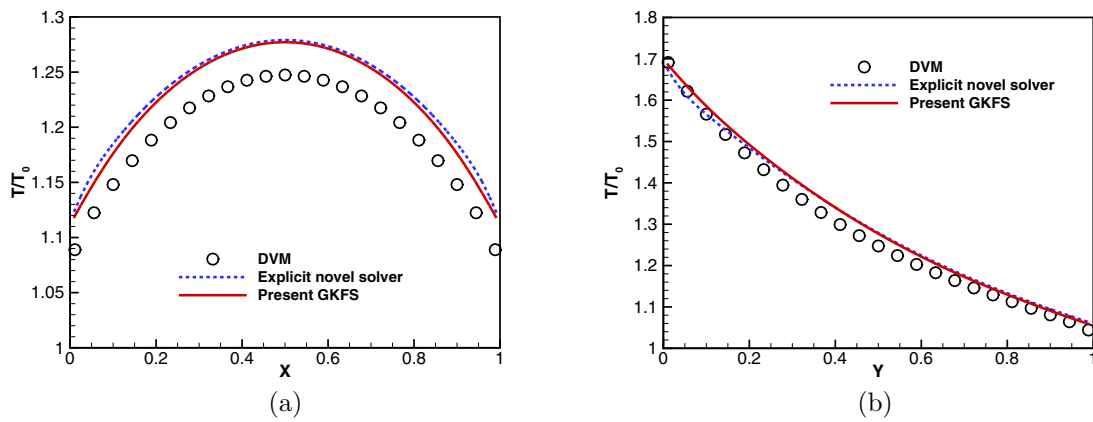


FIG. 34. Comparison of temperature profiles along central line for $Kn = 0.13$: (a) horizontal temperature profiles, (b) vertical temperature profiles.

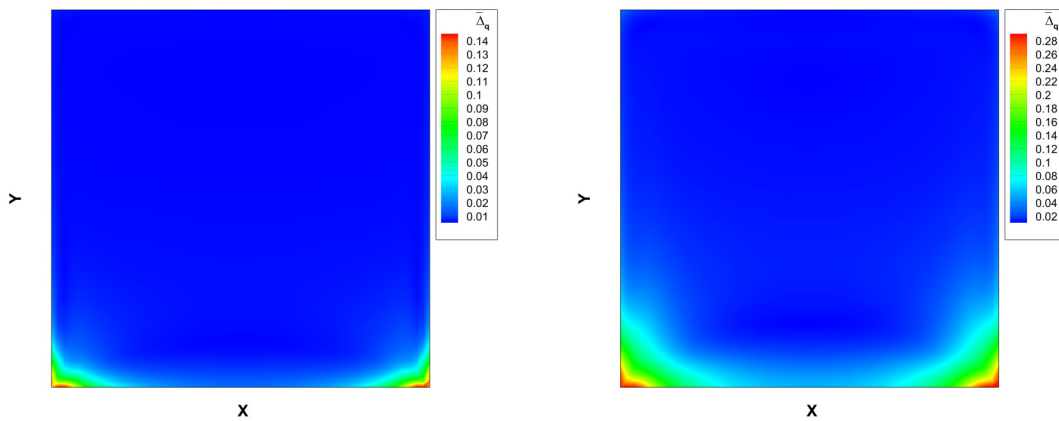


FIG. 35. The contours of $\bar{\Delta}_q$ for $Kn = 0.05$ (left) and $Kn = 0.13$ (right).

VI. CONCLUSIONS

A variant of gas kinetic flux solver is presented for simulation of flows from the continuum regime to the transition regime in this work. The method follows the framework of conventional GKFS and evaluates the numerical fluxes by the moments of distribution function at the cell interface. The key contribution of the present work is the introduction of the correction terms to the stress tensor and heat flux in the approximation of initial distribution function. These correction terms will take effect in the strong nonequilibrium region for flows beyond the NS level. To avoid finding complex expressions or solving complicated partial differential equations for the correction terms, an iterative strategy is proposed. This strategy updates the correction terms by computing the difference between the actual stress tensor–heat flux and linearized ones in the NS level. The present GKFS is validated by three benchmark cases, and simulation

results show that the present solver could not only provide accurate solution in the continuum regime but also capture the strong nonequilibrium effect for flows beyond the NS level. Furthermore, the correction terms for stress tensor and heat flux, $\bar{\Delta}_\sigma$ and $\bar{\Delta}_q$, are calculated, which provide conclusive evidence that the correction terms indeed make contribution in the strong nonequilibrium region, where the linearized constitutive relationship and Fourier’s law are invalid. It is indeed the introduction of correction terms that enables simulation of rarefied flows at moderate Knudsen number.

ACKNOWLEDGMENTS

The research has been supported by the Ministry of Education (MOE) of Singapore (Grant No. MOE2018-T2-1-135), and Natural Science Foundation of Jiangsu Province (Grant No. BK20210273).

-
- [1] D. Pullin, Direct simulation methods for compressible inviscid ideal-gas flow, *J. Comput. Phys.* **34**, 231 (1980).
 - [2] B. Perthame, Second-order Boltzmann schemes for compressible Euler equations in one and two space dimensions, *SIAM J. Numer. Anal.* **29**, 1 (1992).
 - [3] J. Mandal and S. Deshpande, Kinetic flux vector splitting for Euler equations, *Comput. Fluids* **23**, 447 (1994).
 - [4] S. Y. Chou and D. Baganoff, Kinetic flux–vector splitting for the Navier–Stokes equations, *J. Comput. Phys.* **130**, 217 (1997).
 - [5] K. H. Prendergast and K. Xu, Numerical hydrodynamics from gas-kinetic theory, *J. Comput. Phys.* **109**, 53 (1993).
 - [6] K. Xu, L. Martinelli, and A. Jameson, Gas-kinetic finite volume methods, flux-vector splitting, and artificial diffusion, *J. Comput. Phys.* **120**, 48 (1995).
 - [7] K. Xu, A gas-kinetic BGK scheme for the Navier–Stokes equations and its connection with artificial dissipation and Godunov method, *J. Comput. Phys.* **171**, 289 (2001).
 - [8] M. Su, K. Xu, and M. S. Ghidaoui, Low-speed flow simulation by the gas-kinetic scheme, *J. Comput. Phys.* **150**, 17 (1999).
 - [9] K. Xu and H. Liu, Multiscale gas-kinetic simulation for continuum and near-continuum flows, *Phys. Rev. E* **75**, 016306 (2007).
 - [10] L. Yang, C. Shu, and J. Wu, A three-dimensional explicit sphere function-based gas-kinetic flux solver for simulation of inviscid compressible flows, *J. Comput. Phys.* **295**, 322 (2015).
 - [11] L. Yang, C. Shu, and Y. Wang, Development of a discrete gas-kinetic scheme for simulation of two-dimensional viscous incompressible and compressible flows, *Phys. Rev. E* **93**, 033311 (2016).
 - [12] L. Yang, C. Shu, W. Yang, and J. Wu, Development of an efficient gas kinetic scheme for simulation of two-dimensional incompressible thermal flows, *Phys. Rev. E* **97**, 013305 (2018).
 - [13] Y. Liu, L. Yang, C. Shu, and H. Zhang, Three-dimensional high-order least square-based finite difference-finite volume method on unstructured grids, *Phys. Fluids* **32**, 123604 (2020).
 - [14] L. Zhang, Z. Chen, L. Yang, and C. Shu, Double distribution function-based discrete gas kinetic scheme for viscous incompressible and compressible flows, *J. Comput. Phys.* **412**, 109428 (2020).
 - [15] K. Xu and J. C. Huang, A unified gas-kinetic scheme for continuum and rarefied flows, *J. Comput. Phys.* **229**, 7747 (2010).
 - [16] S. Chen, Z. Guo, and K. Xu, Simplification of the unified gas kinetic scheme, *Phys. Rev. E* **94**, 023313 (2016).
 - [17] Z. Guo, K. Xu, and R. Wang, Discrete unified gas kinetic scheme for all Knudsen number flows: Low-speed isothermal case, *Phys. Rev. E* **88**, 033305 (2013).
 - [18] Z. Guo, R. Wang, and K. Xu, Discrete unified gas kinetic scheme for all Knudsen number flows. II. Thermal compressible case, *Phys. Rev. E* **91**, 033313 (2015).
 - [19] M. Torrilhon and H. Struchtrup, Boundary conditions for regularized 13-moment-equations for micro-channel-flows, *J. Comput. Phys.* **227**, 1982 (2008).
 - [20] X. J. Gu and D. R. Emerson, A high-order moment approach for capturing non-equilibrium phenomena in the transition regime, *J. Fluid Mech.* **636**, 177 (2009).
 - [21] Z. Jiang, W. Zhao, Z. Yuan, W. Chen, and R. Myong, Computation of hypersonic flows over flying configurations using a nonlinear constitutive model, *AIAA J.* **57**, 5252 (2019).
 - [22] Z. Y. Yuan, Z. Z. Jiang, W. W. Zhao, and W. F. Chen, Analysis of gas flow over a cylinder at all Knudsen numbers based on non-Newtonian constitutive models, *Int. J. Mod. Phys. B* **34**, 2040076 (2020).
 - [23] S. Liu, Y. Yang, and C. Zhong, An extended gas-kinetic scheme for shock structure calculations, *J. Comput. Phys.* **390**, 1 (2019).
 - [24] D. Burnett, The distribution of molecular velocities and the mean motion in a non-uniform gas, *Proc. London Math. Soc.* **s2-40**, 382 (1936).
 - [25] R. K. Agarwal, K. Y. Yun, and R. Balakrishnan, Beyond Navier–Stokes: Burnett equations for flows in the continuum–transition regime, *Phys. Fluids* **13**, 3061 (2001).
 - [26] W. Zhao, W. Chen, and R. K. Agarwal, Formulation of a new set of simplified conventional Burnett equations for computation of rarefied hypersonic flows, *Aerosp. Sci. Technol.* **38**, 64 (2014).
 - [27] W. Zhao, W. Chen, H. Liu, and R. K. Agarwal, Computation of 1-D shock structure in a gas in rotational non-equilibrium using a new set of simplified Burnett equations, *Vacuum* **109**, 319 (2014).

- [28] K. Xu, Regularization of the Chapman–Enskog expansion and its description of shock structure, *Phys. Fluids* **14**, L17 (2002).
- [29] R. Myong, A computational method for Eu’s generalized hydrodynamic equations of rarefied and microscale gasdynamics, *J. Comput. Phys.* **168**, 47 (2001).
- [30] Z. Yuan, W. Zhao, Z. Jiang, W. Chen, and R. K. Agarwal, Modified nonlinear coupled constitutive relations model for hypersonic nonequilibrium flows, *J. Thermophys. Heat Transfer* **34**, 848 (2020).
- [31] Z. He, Z. Jiang, H. Zhang, and W. Chen, Analytical method of nonlinear coupled constitutive relations for rarefied nonequilibrium flows, *Chin. J. Aeronaut.* **34**, 136 (2021).
- [32] M. Torrilhon and H. Struchtrup, Regularized 13-moment equations: Shock structure calculations and comparison to Burnett models, *J. Fluid Mech.* **513**, 171 (2004).
- [33] Z. Liu, C. Shu, S. Chen, L. Yang, M. Wan, and W. Liu, A novel solver for simulation of flows from continuum regime to rarefied regime at moderate Knudsen number, *J. Comput. Phys.* **415**, 109548 (2020).
- [34] Z. Liu, L. Yang, C. Shu, S. Chen, M. Wan, W. Liu, and Z. Yuan, Explicit formulations of G13-based gas kinetic flux solver (G13-GKFS) for simulation of continuum and rarefied flows, *Phys. Fluids* **33**, 037133 (2021).
- [35] P. L. Bhatnagar, E. P. Gross, and M. Krook, A model for collision processes in gases. I. Small amplitude processes in charged and neutral one-component systems, *Phys. Rev.* **94**, 511 (1954).
- [36] C. Chu, Kinetic-theoretic description of shock wave formation. II, *Phys. Fluids* **8**, 1450 (1965).
- [37] Y. Sun, C. Shu, C. Teo, Y. Wang, and L. Yang, Explicit formulations of gas-kinetic flux solver for simulation of incompressible and compressible viscous flows, *J. Comput. Phys.* **300**, 492 (2015).
- [38] Z. Chen, C. Shu, Y. Wang, L. Yang, and D. Tan, A simplified lattice Boltzmann method without evolution of distribution function, *Adv. Appl. Math. Mech.* **9**, 1 (2017).
- [39] L. Yang, C. Shu, Z. Chen, G. Hou, and Y. Wang, An improved multiphase lattice Boltzmann flux solver for the simulation of incompressible flow with large density ratio and complex interface, *Phys. Fluids* **33**, 033306 (2021).
- [40] Y. Liu, C. Shu, H. Zhang, and L. Yang, A high order least square-based finite difference-finite volume method with lattice Boltzmann flux solver for simulation of incompressible flows on unstructured grids, *J. Comput. Phys.* **401**, 109019 (2020).
- [41] Z. Chen, C. Shu, D. Tan, X. Niu, and Q. Li, Simplified multiphase lattice Boltzmann method for simulating multiphase flows with large density ratios and complex interfaces, *Phys. Rev. E* **98**, 063314 (2018).
- [42] L. Yang, C. Shu, and J. Wu, A simple distribution function-based gas-kinetic scheme for simulation of viscous incompressible and compressible flows, *J. Comput. Phys.* **274**, 611 (2014).
- [43] G. M. Kremer, *An Introduction to the Boltzmann Equation and Transport Processes in Gases* (Springer-Verlag, Berlin, 2010).
- [44] Z. Yuan, L. Yang, C. Shu, Z. Liu, and W. Liu, A novel gas kinetic flux solver for simulation of continuum and slip flows, *Int. J. Numer. Methods Fluids* **93**, 2863 (2021).
- [45] D. A. Lockerby, J. M. Reese, and M. A. Gallis, The usefulness of higher-order constitutive relations for describing the Knudsen layer, *Phys. Fluids* **17**, 100609 (2005).
- [46] Z. Yuan, Z. Jiang, W. Zhao, and W. Chen, Multiple temperature model of nonlinear coupled constitutive relations for hypersonic diatomic gas flows, *AIP Adv.* **10**, 055023 (2020).
- [47] Z. Yuan, W. Zhao, Z. Jiang, and W. Chen, Numerical simulation of hypersonic reaction flows with nonlinear coupled constitutive relations, *Aerosp. Sci. Technol.* **112**, 106591 (2021).
- [48] R. Myong, A generalized hydrodynamic computational model for rarefied and microscale diatomic gas flows, *J. Comput. Phys.* **195**, 655 (2004).
- [49] Z. Jiang, W. Chen, and W. Zhao, Numerical analysis of the micro-Couette flow using a non-Newton–Fourier model with enhanced wall boundary conditions, *Microfluid. Nanofluid.* **22**, 10 (2018).
- [50] D. Wu, D. Wang, and H. Xiao, Nonlinear dissipation and nonequilibrium gas flows, *Phys. Rev. E* **100**, 032101 (2019).
- [51] Z. Yuan, W. Zhao, Z. Jiang, and W. Chen, The application and verification of modified nonlinear coupled constitutive relations model, in *AIAA Scitech 2019 Forum, San Diego, California* (AIAA, Reston, VA, 2019), paper AIAA 2019-1906.
- [52] J. Koellermeier and M. Torrilhon, Numerical solution of hyperbolic moment models for the Boltzmann equation, *Eur. J. Mech. B: Fluids* **64**, 41 (2017).
- [53] G. H. Golub and J. H. Welsch, Calculation of Gauss quadrature rules, *Math. Comput.* **23**, 221 (1969).
- [54] B. Shizgal, A Gaussian quadrature procedure for use in the solution of the Boltzmann equation and related problems, *J. Comput. Phys.* **41**, 309 (1981).
- [55] C. Cercignani and M. Lampis, Kinetic models for gas-surface interactions, *Transp. Theor. Stat.* **1**, 101 (1971).
- [56] W. Liu, Y. Liu, L. Yang, Z. Liu, Z. Yuan, C. Shu, and C. Teo, Coupling improved discrete velocity method and G13-based gas kinetic flux solver: A hybrid method and its application for nonequilibrium flows, *Phys. Fluids* **33**, 092007 (2021).
- [57] C. W. Shu and S. Osher, Efficient implementation of essentially non-oscillatory shock capturing schemes, *J. Comput. Phys.* **77**, 439 (1988).
- [58] J. Qiu and C. W. Shu, Hermite WENO schemes and their application as limiters for Runge–Kutta discontinuous Galerkin method: One-dimensional case, *J. Comput. Phys.* **193**, 115 (2004).
- [59] A. Rana, M. Torrilhon, and H. Struchtrup, A robust numerical method for the R13 equations of rarefied gas dynamics: Application to lid driven cavity, *J. Comput. Phys.* **236**, 169 (2013).
- [60] U. Ghia, K. N. Ghia, and C. Shin, High-Re solutions for incompressible flow using the Navier-Stokes equations and a multigrid method, *J. Comput. Phys.* **48**, 387 (1982).
- [61] A. S. Rana, A. Mohammadzadeh, and H. Struchtrup, A numerical study of the heat transfer through a rarefied gas confined in a microcavity, *Continuum Mech. Therm.* **27**, 433 (2015).
- [62] L. Yang, C. Shu, J. Wu, and Y. Wang, Numerical simulation of flows from free molecular regime to continuum regime by a DVM with streaming and collision processes, *J. Comput. Phys.* **306**, 291 (2016).